© Copyright 2019

Kenneth Lao Chen

Divergent Single-Cell Trajectories in Homeostatic Control and Genome Instability during Aging

Kenneth Lao Chen

A dissertation

submitted in partial fulfillment of the

requirements for the degree of

Doctor of Philosophy

University of Washington

2019

Reading Committee:

Matt Kaeberlein, Chair

Marshall Horwitz

Michael MacCoss

Program Authorized to Offer Degree:

Genome Sciences

University of Washington

Abstract

Divergent Single-Cell Trajectories in

Homeostatic Control and Genome

Instability during Aging

Kenneth Lao Chen

Chair of the Supervisory Committee:
Matt Kaeberlein
Departments of Pathology and Genome Sciences

The budding yeast has a long and storied history as a model organism for biological inquiry. Accordingly, experiments into the replicative aging of *S. cerevisiae* have yielded critical insights into evolutionarily conserved mechanisms of aging. Historically, replicative aging experiments have relied on labor-intensive techniques for lifespan measurement, and methods to observe physiological function across a cell's lifespan were not available. Recently, novel microfluidic devices have been developed for the whole-lifespan monitoring of yeast cells during replicative aging. Using time-lapse microscopy, these devices allow researchers to measure replicative

lifespan in much higher throughput and to quantitate various aspects of cell biology during aging, with single-cell resolution, across a cell's entire lifetime. In this dissertation, I engineer a low-cost motorized light microscopy system with open-source software, aimed at increasing the accessibility this new technology. Recently, an early life decline in vacuolar/lysosomal acidity in the budding yeast has been found to underlie the aging process. I use our microfluidic device to investigate the consequences of lysosomal/vacuolar dysfunction during yeast replicative aging. I find that this loss acidity triggers an iron sulfur cluster deficiency and is associated with a age-associated genome instability. However, only a subset of cells mount the expected iron starvation gene expression program, leading to divergent single-cell trajectories of iron dyshomeostasis during aging. Cells which mount an iron starvation response during aging have limited iron sulfur cluster deficiency and extended survival and passage through periods of genome instability during aging.

TABLE OF CONTENTS

LIST OF FIGURES

LIST OF TABLES

ACKNOWLEDGEMENTS

Thank you to all the members of the Kaeberlein lab during my time here, to the UW MSTP, and to the departments of Pathology and Genome Sciences. To my friends and family, thank you for all of your support throughout my life. To my classmates, especially Aaron Seo, BJ Valente, and Michael Doud, thank you for your years of friendship and camaraderie in making Seattle a new home.

DEDICATION

For my parents Mary and Zhao, thank you for your boundless love and inspiration

Chapter 1. INTRODUCTION

This chapter is adapted from a published paper:

Chen, K. L., Crane, M. M. & Kaeberlein, M. Microfluidic technologies for yeast replicative lifespan studies. Mechanisms of Ageing and Development 161, Part B, 262–269 (2017).

1.1 HISTORICAL METHODOLOGY

Although budding yeast colonies can be propagated indefinitely, in 1959, Mortimer and Johnson reported that individual yeast cells are not immortal. *S. cerevisiae* cells reproduce clonally but asymmetrically, with a smaller daughter cell budding from its larger mother [1]. Mortimer and Johnson closely monitored individual mother cells grown on an agar pad and periodically used a micromanipulator to manually remove mature daughter buds. This removal of daughter cells is necessary because a single mother cell becomes indiscernible from its exponentially dividing progeny after only a handful of division cycles. In this seminal study, they reported that an individual mother cell can divide only a finite number of times—its replicative lifespan. Since then, multiple conserved longevity pathways have been discovered in the budding yeast [2]. With a short generation time, genetic tractability, and minimal husbandry costs, the budding yeast has become a premier model organism for aging research [3]. Mortimer and Johnson's microdissection technique, developed over fifty years ago, remains the bread-and-butter yeast aging assay [4]. Unfortunately, it is also time and labor intensive. As a consequence, many labs forgo replicative lifespan studies and, even among those that perform them, sample sizes are often too small for rigorous statistical confidence in published results. For example, the only genome-wide analysis of replicative lifespan performed to date utilized an iterative strategy involving lifespan analysis of only 5 cells per deletion strain [5]. Thus, in many ways, the standard replicative lifespan assay has become a rate-limiting step in the progress of yeast aging research.

Recently, a number of groups [6–11] have developed microfluidic technologies to address this problem (Table 1.1). Microfluidic devices refer to a diverse class of objects featuring sub-millimeter chambers and channels. At this scale, fluids have interesting mechanical properties—

such as laminar flow—which allow researchers to precisely manipulate tiny volumes of liquid for applications including bioassay integration, high throughput screening, and chemical synthesis among many others [12,13]. Devices constructed from polydimethylsiloxane (PDMS)—a clear, gas-permeable, and biocompatible elastopolymer—have proven particularly useful for cell biology. Tiny cell culture chambers with precisely controlled cellular microenvironments can be created by sealing PMDS blocks with micron-sized surface features onto glass cover slips.

A wide variety of microfluidic devices, including a commercial platform, have been developed for yeast culture and investigation [14–17]. Most, however, are only suitable for experiments lasting a few hours or less. Though earlier attempts were made to apply microfluidics to yeast aging research [18], the first device to successfully demonstrate the ability to perform a replicative lifespan analysis was published in 2012 [10]. Since then, multiple additional microfluidic designs with lifespan analysis capabilities have been developed [6–9,17,19]. The devices developed for yeast aging feature clever geometrical structures to mechanically trap mother cells. These structures exploit the size difference between mother cells and newborn daughter cells or the budding patterns of mother cells, generally allowing fluid flow to selectively remove mature daughters. The effective removal of undesired cells is crucial to prevent the device from becoming overgrown with multiplying progeny. When coupled with time-lapse microscopy, these devices allow both measurement of replicative lifespans and observation of physiological changes as the trapped cells age. Lifespans in microfluidic devices at standard 30 °C conditions last 2 – 5 days. (In contrast, microdissection experiments can last several weeks, as mother cells are generally permitted to undergo fewer than a handful of divisions per day and refrigerated overnight to

prevent overgrowth.) The following text will discuss these seven microfluidic devices for the whole-lifespan trapping and monitoring of budding yeast cells.

1.2 NOVEL METHODOLOGIES: CURRENT MICROFLUIDIC DEVICE DESIGNS

Chemical and Mechanical trapping

The first microfluidic device developed to perform a replicative lifespan experiment was published by Xie and colleagues in 2012 [10]. This device uses both mechanical constraints and biotin-avidin affinity (Figure 1.1A). In this device, the height of the trapping chamber is 4 μm, approximately the diameter of a yeast cell. Additionally, the glass surface is functionalized with biotinylated bovine serum albumin followed by neutravidin. Prior to loading into the device, cells are labeled with biotin. Because daughter cell walls are generated anew, only the mother cells retain this surface mark. After loading, mother cells are immobilized both mechanically—squeezed between the PDMS ceiling and the glass floor of the chamber—and chemically—glued to the glass floor by the interaction of the cell's biotin and the device's avidin. Fluid flow preferentially removes the smaller, biotin-free daughter cells. Yeast replicative lifespan curves were successfully generated using this device; however, those lifespans were shorter (see **Table 1.2**) than the results seen from microdissection experiments on agar plates [10] .

Vertical mechanical trapping by pensile columns/micropads

Later in 2012, two groups published very similar device designs using purely geometric measures to selectively trap mother cells [6,8]. In these designs, the trapping chamber does not have

a uniform height. “Micropads” (30 by 15 μm, Lee et al.) or “pensile columns” (40 by 40 μm, Zhang et al.) descend from the PDMS ceiling to create areas where the floor to ceiling distance is only 4-5 μm (Figure 1.1B). Between the micropads/columns, the trapping chamber is much taller (15 μm for Lee et al., unspecified for Zhang et al.) Cells are loaded at high pressure, pushing the column areas upwards temporarily and allowing cells to flow underneath. When this pressure is released, the cells are trapped, sandwiched under the micropad above. Again, mother cells are preferentially retained over the smaller daughters because of the size difference. Moreover, the limited area of the micropad/column prevents overgrowth, as progeny that grow into the non-micropad areas are no longer vertically constrained and more easily washed out. However, Lee et al. reported that over 70% of cells were lost before the end of their experiments. Retention data was not reported by Zhang et al.

Trapping in elongated cavities

The CLiC (Cell Loaded into a Cavity) device features “trapping areas” (90 by 40 μm, 3.3 μm height) arranged in a grid and separated by media flush channels (40 μm height) [11]. Each trapping area features two elongated “cavities” or dead-end hallways that run off of the main trapping area (6 or 10 by ~32 μm) (Figure 1.1C). This design requires a significantly larger footprint per trapped mother cell than the other devices. This may become an issue in experiments that require a large number of cells (e.g. investigating rare events) when the speed of the microscope components becomes a limiting factor. Cells are loaded through the media flush channels such that a handful are caught within each trapping area. Subsequent cell division results in a confluent monolayer of cells in the trapping area that eventually deposits a new virgin

cell (never having previously produced a daughter cell) at the dead-end tip of the elongated cavity. This method has the advantage that cells are guaranteed to be virgin at the beginning of the lifespan experiment, while the previous three designs are unable to control this [11]. In a log-phase culture, one would expect about half of the cells to be virgin daughters and less than 1/16 of the cells to have budded more than three times. Staining of bud scars showed that the average age of a trapped cell under a pensile column in Zhang et al. is less than two divisions at the start of an experiment [8].

The CLiC device depends on the unipolar axial budding pattern of haploid yeast cells in the BY strain background [11]. It is worth noting that this device, along with all devices described in this review have only been demonstrated for lifespan analyses of haploid cells and may be unsuitable for larger diploid cells, as discussed further below. If a cell at the dead-end tip of the cavity buds towards the exit, it will continue to bud in the same direction and tend to remain trapped in the cavity for its entire replicative lifespan. The limited width of the cavity ensures that daughters and further progeny are continuously pushed out of the cavity. Although cells can rotate and polarity switches occur occasionally, the authors reported retention of ~65% of trapped mother cells for their entire replicative lifespans [11].

Trapping between two columns

The ALCATRAS (A Long-term Culturing and TRApping System) device utilizes traps each composed of two floor-to-ceiling columns arranged with a "\ /" shaped footprint (Figure 1.1D). When a cell suspension is flowed into the device, individual cells are caught between the two

columns. Continuous, unidirectional fluid flow keeps each mother cell immobilized against the columns. The limited height of the device chamber discourages vertical stacking of cells. Like the designs described above, this device exploits the size difference between mother and daughter cells. Daughter buds are forced downstream through the gap between the two columns, detaching when mature. Buds that emerge upstream are similarly removed by fluid flow upon maturity, and the authors reported whole-lifespan retention of ~40-60% of trapped mother cells. The ALCATRAS device also does not guarantee that mothers begin the experiment as virgins. However, unlike all the previously described devices, which have non-uniform internal heights, the mold for this device requires features of only a single height[9].

The HYAA-Chip (High-throughput Yeast Aging Analysis) follows essentially the same principle as the ALCATRAS device, sharing the advantages of single-layer fabrication and small trap footprint. However, the cross-section of the floor-to-ceiling columns is different, as is the spacing between columns in a single trap and between traps (Figure 1.1E). This resulted in reports of >90% retention of wild-type mother cells for their entire lifespans [7]. This device and trapping structure has been validated on a number of both long- and short-lived mutants (Table 1). The trapping mechanism used in both of these papers allows a higher density of cells to be imaged within a single field of view when compared with the previous designs.

Trapping in a three-column jail

The Yeast Replicator device also uses vertical floor-to-ceiling columns to trap individual cells, modifying an earlier three-column "jail" design [19] (Figure 1.1F). The three columns, arrayed at

the vertices of an equilateral triangle, create a fully constrained trapping area for a single cell. When cells are loaded into the device, they are first caught between two columns outside the jail. These temporarily immobilized cells can then bud into the central trapping area. When mature, the buds become the trapped mother cells. Like the CLiC device, the Yeast Replicator guarantees that trapped cells start in the device as virgins. Daughter buds of these trapped cells emerge in between the three columns of the jail and are washed away when mature. Retention rates were not reported by the authors [14].

1.3 RECENT DISCOVERIES

Coupled with time-lapse microscopy, these devices allow researchers to more easily collect replicative lifespan data. Moreover, when combined with fluorescently-labeled proteins or dyes, researchers can track changes in cell physiology (e.g. organelle structure or function [6,20], protein level or localization [21], promoter activity [10], daughter-cell characteristics [22]) across the aging process. Importantly, these measures can be associated at single-cell resolution with lifespan or other age-associated changes (e.g. cell cycle duration). A number of interesting observations have followed. For example, researchers found that delays in nuclear segregation during cytokinesis occur rarely during a cell's lifetime but increase dramatically in frequency after division speeds slow with age [23]. Researchers also correlated heterogeneity in end-state cell morphology, which had been previously reported by microdissection studies [24], with molecular properties of those cells. Cells trapped under a PDMS column that die in a round (as opposed to elongated) morphology are shorter-lived, display more pronounced measures of mitochondrial dysfunction, and have higher Hsp104 promoter activity at death [6,8]. This suggests that each yeast cell may experience one of multiple modes of cellular death. Interestingly, another report using

paired-column traps correlated lifespan with the morphology of the attached daughter bud at cell death (round, elongated, or no bud) but made no mention of elongated mothers [7]. This suggests that the geometry of the trapping structure may affect trends in aged cell morphology.

Building on the widely mentioned observation that cell cycle durations increase dramatically during the last few cell divisions [11,19], Xie *et al.* found that mutants defective in telomerase function display stochastic episodes of cell-cycle lengthening in young cells. These strains are short-lived, display aged mitochondrial morphology, and activate more frequent bursts of DNA damage response throughout life. Interestingly, lifespan shortening is unrelated to telomere length [22]. Xu et al. made similar observations when tracking cellular lineages instead of mother cells. They observed a subpopulation of lineages that experienced stochastically (but not progressively) elongated cell divisions, linking this behavior to Pol32 DNA damage repair activity [25].

Mitochondrial membrane potential has previously been implicated as a biomarker or mediator of age-related cellular pathology [26–29]. By tracking the mitochondrial membrane potential in individual cells across the aging process, Fehrmann et al. found that the instantaneous risk of losing mitochondrial membrane potential did not increase with age. Moreover, they reported that the cells who eventually lost mitochondrial membrane potential were not significantly shorter-lived than those who maintained high mitochondrial potential for their entire lifespans [11]. These types of observations are wholly dependent on the ability to follow single cells and observe their physiological states through the entire aging process.

1.4 CONSIDERATIONS AND LIMITATIONS

Because lingering progeny cells will divide and proliferate exponentially, microfluidic lifespan devices must effectively clear the vast majority of daughter cells to keep the device from becoming clogged with cells. Thus, a very delicate balance must be struck between retention of mother cells and removal of unwanted progeny. The key innovation of most of these devices is a geometry that exploits the size difference between mother and daughter cells to immobilize aging mothers and wash away new daughter cells. And as such, all designs are very sensitive to the size of the mother. All devices mentioned in this review have focused on haploid cells, and although the size difference and altered budding pattern of diploids doesn't ensure failure, so far none of these devices have been tested on diploid cells. While this may not be a severe limitation to the utility of such devices, it is clear that ploidy can impact replicative lifespan in yeast (for example BY4743 diploids are longer-lived than the corresponding haploid strains) , and aging studies in nearly every other model system are performed in diploid organisms [30]. Moreover, even within haploids, this balance is complicated by several factors. Mother and daughter cells are nearly identical in size during the first division or two. The device needs to be able to trap these small mother cells effectively at the beginning of the experiment. However, over the course of their lifespans, old mother cells can grow to be multiple times the size of young mother cells. The trapping geometry needs to accommodate these much larger cells as well, as excessive pressure on cells can induce stress responses and may reduce lifespan [10,19]. Daughters of old mother cells are also larger [31], and it is unknown whether pressure on growing buds (constrained between two columns in some designs) can affect the aging process. Additionally, a large daughter bud can dislodge its mother from a trap, and multiple buds sometimes remain attached to the mother cell in a clustered arrangement, further complicating

the designs. Judgment of the success of many of the published devices in overcoming these obstacles is difficult due to the lack of raw data available (i.e. time-lapse videos showing the whole device or an entire field of view). Indeed, the devices mentioned in this review have widely varying trends for mother cell retention through time (see Table 1.1).

An experiment where most of the cells are lost before senescence is not necessarily a failure. Statistical right-censoring to utilize partial lifespan data (i.e. a mother cell that is retained for several divisions but washed out before senescence) is routinely used in survival analysis [32]. However, the reasoning that undergirds this method assumes that cells disappearing before senescence are not systematically different than those trapped for their entire lifespans. The fact that these devices exploit cellular size or budding characteristics to trap mother cells is a strong indicator that this requirement may not be upheld. Moreover, as cells continue to grow in volume over their entire lifespans, published work has suggested that cell size may be a biomarker of remaining lifespan [33]. Thus genetic or environmental interventions that affect lifespan through pathways that also affect cellular budding patterns or geometry may not be suitable for study in some devices. This may be a particularly important limitation, given that many genetic and environmental interventions that extend lifespan also affect mother cell size [33,34].

Thus far, studies have not attempted to demonstrate robustness of lifespan results to microfluidic-specific experimental conditions such as fluid speed, culture growth phase, or pre-loading treatments such as sonication or centrifugation. Some of the published devices have reported lifespans both for wildtype cells, and a small number of short- and long-lived strains that are comparable to those measured by microdissection (Table 1.2 and 1.3). However, a major limitation of the current literature in this area is that no studies have assessed the ability of any microfluidic device to recapitulate the reported longevity effects of a large number of longevity-

altering interventions. In one case, Huberts *et al.* reported that the longevity-promoting effect of caloric restriction is not seen in their microfluidic design. Their observations were accompanied by an interesting meta-analysis showing that studies showing the protective effects of dietary restriction in yeast generally reported control populations that were shorter-lived than the norm [35]. Later, Jo *et al.* found that dietary restriction does increase longevity in cells aged in their device, noting that the conclusions of Huberts *et al*. were drawn from lifespan experiments in which ~85% of initial population was censored [7].

Going forward, it will be important to establish which microfluidic device designs, and under what experimental conditions, most closely recapitulate the results obtained using the "gold standard" microdissection assay across a spectrum of genetic and environmental conditions. This is particularly true in those cases where the yeast replicative aging model has been found to recapitulate the effects of analogous interventions in multicellular eukaryotes, such as *C. elegans* [36,37]. Key pathways that should be explored in detail include the ability of yeast cells to show lifespan extension from dietary restriction (both glucose and other nutrients) and the response to conserved genetic modifiers of aging such as sirtuins and the target of rapamycin (TOR).

1.5 THESIS OUTLINE

Chapter 2

In this chapter I discuss the engineering of a low-cost light microscopy system to collect whole-lifespan time-lapses of aging cells in microfluidic devices. Aside from concerns about device

performance, adoption of these devices can be difficult for labs without previous microfluidics expertise. Authors are happy to share blueprints of the photomask, which can then be purchased from a number of sources. However, to manufacture the device molds using the photomasks, a nanofabrication facility is required. Further, use of these devices has been largely limited to laboratories with access to expensive motorized microscopes. These microscopes allow researchers to parallelize experiments, capturing lifespans of multiple strains at once (through device design or the use of multiple devices at once). However, priced at tens of thousands of dollars, they can often be outside the budget of researchers dependent on the low cost of yeast research. Because experiments require continuous monitoring for upwards of 2 days, core facility rates can also be unaffordable. Towards this end, we have developed a low-cost microscopy system based on commercially available budget-microscopes and open-sources software that can capture whole-lifespan time-lapses.

Chapter 3

In this chapter, I discuss the application of our microfluidic device to the investigation of lysosomal dysfunction, iron metabolism, and genome instability during aging. The loss of vacuolar/lysosomal acidity is an early initiator of homeostatic decline during aging [26,38]. Here, we use yeast genetics, microfluidics, and single-cell imaging to investigate the connections between vacuolar acidity, iron homeostasis, and genome instability during aging. We find that, akin to vacuolar ATPase (*vma*) mutants—which are unable to acidify the vacuole—aged cells suffer from genome instability and iron sulfur cluster insufficiency. However, only a subset of an isogenic, environmentally homogenous population mounts the expected activation of the iron

regulon (IR) against this deficiency, resulting in divergent trajectories of iron homeostasis during aging. Iron sulfur clusters are essential cofactors for DNA polymerases and many DNA repair proteins, and we find that the IR-active trajectory is characterized by extended passage and survival through a genome unstable state during aging.

1.6 FIGURES AND TABLES

Table 1.1. Key differences between microfluidic devices

Publications Grouped by Device	**Trapping Method**	**Strains per Device**	**Mother Retention**	**Ensure Virgins**	**Single Trap Footprint***	**Mutant Strains Tested for Lifespan**	**Raw Data Provided**
Xie et al. 2012 Rafelski et al. 2012	Height restriction + Chemical	8	Not Reported	No	N/A, "3-5 cells per field of view"	*fob1Δ* *ypt11Δ*	Videos of entire field of view
Lee et al. 2012	Pensile Column/ Micropad	4	30%	No	Single pad: 450 μm^2 With spacing: ~850 μm^2 (up to 2 cells/trap)	*fob1Δ* *sir2Δ*	Videos of single traps
Zhang et al. 2012 Xie et al. 2015	Pensile Column/ Micropad	1	15-30%	No	Single column: 1600 μm^2 Spacing not reported (up to 2 cells/trap)	*est2*-D530A *fob1Δ* *mrc1^{AQ}* *sir2Δ* *sml1Δ* *tel1Δ* *tlc1Δ* *mec1Δsml1Δ* *mrc1^{AQ}tlc1Δ* *rad9Δtlc1Δ* *rad52Δsml1Δ* *sml1Δtlc1Δ* *tel1Δtlc1Δ* *mrc1^{AQ}Δtel1Δtlc1Δ* *rad52Δsml1Δtlc1Δ*	Videos of single traps
Fehrmann et al. 2013 Meitinger et al. 2014	Elongated Cavities	1	~65%	Yes	Single trapping area: ~3840 μm^2 (up to 2 cells/trapping area)	*nba1Δ* *rga1Δ* *nba1Δrga1Δ*	Videos of single traps
Crane et al. 2014	2-Column Traps	1	40-60%	No	Single trap: ~100 μm^2, With spacing: ~750 μm^2	*bre1Δ* *bre1Δ* None	Video of entire chip
Jo et al. 2015	2-Column Traps	16	>90%	No	Single trap: ~200 μm^2 With spacing; ~700 μm^2	*bre1Δ* *chl1Δ* *fob1Δ* *hsp104Δ* *idh1Δ* *rpl22aΔ* *rpn4Δ* *sas2Δ* *sip2Δ* *tma19Δ* *tor1Δ* *ubr2Δ*	Videos of single traps
Liu et al. 2015	3-Column Jails	10	Not Reported	Yes	Single trap: ~175 μm^2 With spacing: 1788 μm^2	*fob1Δ* *sgf73Δ* *tor1Δ* *sir2Δ* *gpa2Δ* *rpl31aΔ*	Photos of single cells of unknown age

*Actual number of trapped mother cells/field of view is highly dependent on loading protocol including density of seeding culture, injection force, and length of seeding period. Often, optimal filling of traps must be balanced against having too many cells per trap or a greater chance of cells caught in non-trap areas leading to overgrowth of device.

Table 1.2. Wildtype lifespans in different device designs

Reporting Publication	Trapping Principle	Running Media	Growth Conditions Prior to Loading[+]	Strain	Lifespan*
Xie et al. 2012	Mechanical + Chemical	YPD	grown in YPD	BY4741	median ≈ 17
Lee et al. 2012	Pensile Column/ Micropad	YPD or Synthetic Defined with 2% glucose	grown overnight to stationary phase, diluted to OD_{600} = 0.3, incubated 3h at 30 °C, sonicated mildly	"BY"	median = 25
Zhang et al. 2012	Pensile Column/ Micropad	Not Reported	grown in YPED at 30 °C overnight to OD_{600} = 1.0, diluted 1: 50, incubated 6 h at 30 °C	BY4741 BY4742	BY4741: mean = 23.6 BY4742: mean = 26.0
Fehrmann et al. 2013	Elongated Cavities	Synthetic Complete with 2% glucose (SC)	"… grown overnight, transferred to fresh medium the next morning, and allowed to grow to log phase until transfer to the microfluidic device in the afternoon."	BY4741	Including right-censored cells: median = 32.4 Including only cells seen to die: median = 25.3
Crane et al. 2014	2-Column Traps	XY with 2% glucose	grown overnight in XY with 2% glucose "and then diluted and allowed to grow to log phase…"	S288C	mean = 22.4
Jo et al. 2015	2-Column Traps	YPD, Synthetic Complete with 2% glucose (SC)	"… cultured in YPD at 30 °C overnight before diluting 10–50-fold and loading…"	BY4741	YPD: mean = 26.76 SC: mean = 24.16
Liu et al. 2015	3-Column Jails	YPD, CSM with 2% glucose	grown overnight in CSM with 2% glucose to final density of 0.25	"BY"	YPD: mean = 22.2 CSM: mean = 24.2

Reported lifespans of wild-type haploid cells in each microfluidic device. *Approximate values are estimated from survival curves. [+]Includes all details specified in the publication

Table 1.3. Reported mutant lifespans in different device designs

Strain	**Microfluidic Lifespan**	**Microdissection Lifespan**
bre1Δ	17.2 (Jo et al. 2015)	17.6
chl1Δ	19.3 (Jo et al. 2015)	
est2-D530A	7.6 (Zhang et al. 2015)	
fob1Δ	~29 (Xie et al. 2012) 33.1 (Zhang et al. 2012) 33.9 (Jo et al. 2015) 31.0 (Liu et al. 2015)	36.0
gpa2Δ	29.9 (Liu et al. 2015)	32.0
hsp104Δ	26.0 (Jo et al. 2015)	32.4
idh1Δ	27.9 (Jo et al. 2015)	33.5
mrc1^{AQ}	~25 (Zhang et al. 2015)	
nba1Δ	14 (Meitinger et al. 2014)	
rga1Δ	12 (Metinger et al. 2014)	
rpl22aΔ	30.0 (Jo et al. 2015)	35.8
rpl31aΔ	30.6 (Liu et al. 2015)	34.6
rpn4Δ	18.1 (Jo et al. 2015)	13.3
sas2Δ	31.8 (Jo et al. 2015)	32.4
sgf73Δ	29.6 (Liu et al. 2015)	42.2
sip2Δ	28.6 (Jo et al. 2015)	31.1
sir2Δ	15.4 (Zhang et al. 2012) 13.3 (Jo et al. 2015) 12.7 (Liu et al. 2015)	13.3
sml1Δ	~27 (Zhang et al. 2015)	
tel1Δ	~27 (Zhange et al. 2015)	
tlc1Δ	12.6 (Zhang et al. 2015)	
tma19Δ	27.3 (Jo et al. 2015)	33.4
tor1Δ	29.0 (Jo et al. 2015) 30.7 (Liu et al. 2015)	29.6

ubr2Δ	31.2 (Jo et al. 2015)	40.9
ypt11Δ	Bimodal, overall mean unspecified (Rafelski et al. 2012)	
mec1Δsml1Δ	~20 (Zhang et al. 2015)	
mrc1^{AQ}tlc1Δ	8.8 (Zhange et al. 2015)	
nba1Δrga1Δ	6 (Meitinger et al. 2014)	
rad9Δtlc1Δ	16.5 (Zhang et al. 2015)	
rad52Δsml1Δ	~12 (Zhang et al. 2015)	
sml1Δtlc1Δ	~22 (Zhang et al. 2015)	
tel1Δtlc1Δ	9.8 (Zhang et al. 2015)	
mrc1^{AQ}Δtel1Δtlc1Δ	11.5 (Zhang et al. 2015)	
rad52Δsml1Δtlc1Δ	~7 (Zhang et al. 2015)	

Microdissection lifespan values for all strains tested in Jo et al. 2015 were sourced from its own supplemental information, which cites other primary literature. Other microdissection lifespan values were sourced from McCormick et al. 2015 [6]. Values to the tenth precision indicate mean. Whole numbers indicate median. Tilde indicates median estimated from survival curve.

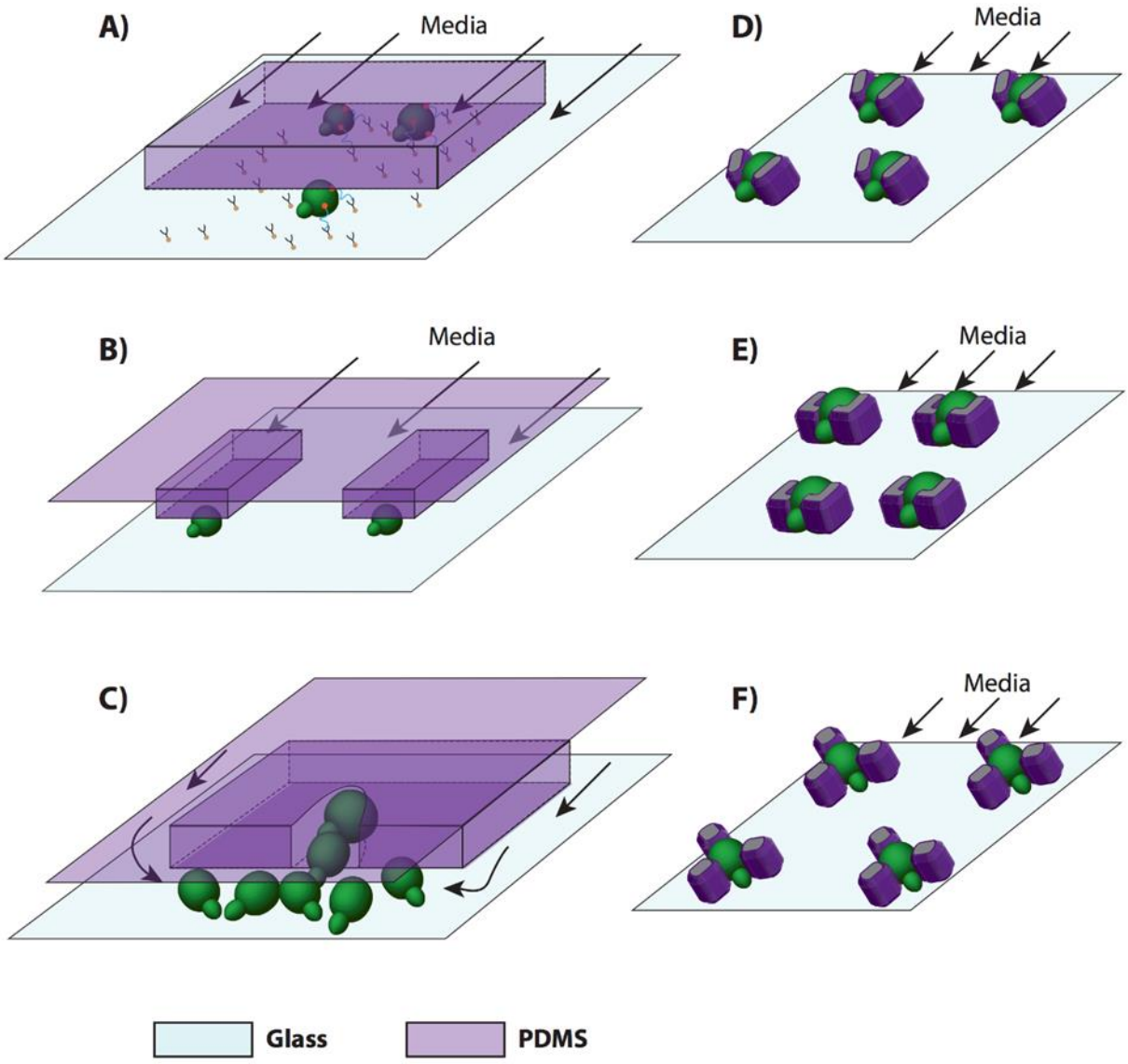

Figure 1.1. Microfluidic device designs

A) This device relies both on a shortened confining ceiling, and chemical bonds. The surface of the glass is coated in streptavidin, and all the mother cells are labeled with biotin. This not only confines the cells vertically, but bonds them chemically to the surface. B) Two groups independently developed devices that rely solely on confinement under small columns or micropads. These small regions physically restrain the larger mothers, but allow the newborn daughters to wash away. C) CLiC device. This constrains the cells in both the vertical dimension,

and places the mother cell in a narrow, elongated cavity in the wall. A small confluent monolayer of cells grows around the cavity, but once the region is full, cells are pushed out and washed away by the bypass channels. D) ALCATRAS device design. A small set of PDMS pillars in a V-shape traps the larger mother cells, and allow daughters to bud through the opening and be washed away. E) HYAA device design. A pair of L-shaped PDMS pillars traps mother cells and allows daughters to be removed by flow. F) Yeast Replicator device design. A small PDMS jail composed of three square pillars traps small newborn daughters and holds them. New daughters bud outside the trap and are washed away.

Chapter 2. BUDGET MICROSCOPY FOR YEAST MICROFLUIDIC AGING STUDIES

This chapter is adapted from a manuscript submitted for publication:

Chen, K. L., Ven, T. M., Crane, M. M. , Chen, D. E., Feng, Y. C., Suzuki, N., Russell, A. E., Moraes, D., & Kaeberlein, M. A budget light microscopy system for yeast microfluidic aging studies. *Under Review*

2.1 ABSTRACT

Recently, microfluidic technologies have been developed to allow higher throughput collection of yeast replicative lifespan data. Adoption of these devices has been limited, in part, due to the high cost of the motorized microscopy instrumentation from mainline manufacturers. Inspired by recent development of open source microscopy hardware and software, we developed minimal-cost hardware attachments to provide long-term focus stabilization for lower-cost microscopes and open source software to manage concurrent time-lapse image acquisition from multiple microscopes. We hope that these tools will help spur the wider adoption of microfluidic technologies for the study of aging in yeast.

2.2 INTRODUCTION

The finite replicative lifespan of budding yeast cells was first reported by Mortimer and Johnson in 1959 [1]. *S. cerevisiae* cells divide asymmetrically, segregating age-accumulated damage and producing a smaller, rejuvenated daughter cell. Mortimer and Johnson monitored individual mother cells grown on an agar pad. To maintain observation of the original cells, they manually removed mature daughter cells using a micromanipulator, preventing the accumulation of an exponentially growing population.

Since then, countless researchers have exploited the scientific convenience and minimal husbandry costs of the budding yeast to discover multiple conserved longevity pathways [2,3,39]. The gold standard for the collection of yeast replicative lifespan data remains Mortimer and Johnson's microdissection technique. Unfortunately, this method is a time- and labor- intensive task. Consequently, insufficient sample sizes are common in replicative lifespan studies, and many labs avoid performing replicative aging experiments. There is only one genome-wide

replicative lifespan study to date, which was only made feasible by utilizing a strategy that initially filtered the deletion collection using lifespan analysis of only 5 cells per deletion strain [5]. In some ways, the microdissection assay may be a bottleneck that limits progress of aging research in the budding yeast.

In the last few years, several microfluidic devices have been developed to automate the microdissection process [6–11,19,40,41]. These devices generally feature structures that exploit the size difference between mother and daughter cells or the unipolar budding patterns of haploid yeast cells to mechanically trap mother cells. Use of these devices allows advantages over traditional microdissection—fluid flow automates the removal of progeny replacing hours of manual labor, the tiny size of the device traps allows for the concurrent monitoring of hundreds of cells, and the continuous nature of the progeny removal shortens the data collection time from several weeks to several days. These devices have already been used to make important discoveries about aging biology [22,35,42–45]. However, utilization has been limited to only a handful of laboratories, most of which are the developers of the original devices or close collaborators at the same institution. One reason for the limited use of microfluidic devices among the yeast research community is the expertise and clean-room equipment needed to fabricate the molds used to produce these devices. Once molds have been fabricated, however, generation of devices from those molds is both facile and affordable [46]. Another reason is the cost of microscopy. Studies utilizing microfluidic devices for yeast aging have generally used expensive motorized inverted microscopes from the traditionally well-known manufacturers [21,22,35,40]. Costing tens of thousands of dollars, they are often outside the budget of many labs interested conducting regular yeast aging studies.

Recently, multiple open-source designs have been published for microscopy hardware and software. These resources include designs for highly sophisticated light-sheet[47] and two-photon[48] microscopes, motorized accessories[49], cell-phone extension[50–52], and a design with production costs below $1[53] . Inspired by these advances, we developed simple hardware attachments and open-source software that facilitates the facile and reliable collection of brightfield images for yeast replicative lifespan data on consumer-grade microscopes with a total system cost of less than $1,000 (Figure 2.1).

2.3 DESIGN

Our goal was to develop a low-cost, light microscopy system to reliably measure yeast replicative lifespan using a microfluidic device. In order to measure lifespan in this way, it is necessary to acquire multi-day time-lapses comprised of high-resolution brightfield images of yeast mother cells (roughly 3-10 um in diameter) aging in a microfluidic device. Replicative lifespan can then be quantified by counting the number of daughter cells that are produced by each trapped mother cell throughout the course of the experiment.

A central challenge in long term microscopy imaging experiments is maintaining the sample in focus against vertical stage drift caused by thermal fluctuations, mechanical slack in the focus system, or other sources of tension. Automated compensation is possible if the distance between the objective and sample can be adjusted via motorized microscope components. To this end we had a wide array of microscopy hardware solutions to choose from. In choosing what design strategy to pursue, we wanted to balance several potentially conflicting priorities: cost,

convenience, and performance. On one end of the spectrum, popular motorized microscopes from the traditional microscope manufacturers offered an expensive but highly convenient solution. These microscopes and the accompanying software offer both image-based computational autofocus as well as hardware attachments that continually measure the distance between objective and sample. With strong technical support and a well-documented history of high experimental performance, these solutions represented the high performance, high cost, high convenience end of the spectrum. On the other end, instructions for completely built-in-house motorized microscopes could also be found on the internet and in multiple peer-reviewed scientific journals[48,49,54,55]. Many of these were low cost and varied in complexity and performance. To create an economical solution that could be easily adopted by a wide variety of laboratories with minimal engineering expertise, we chose to balance the convenience, cost, and performance of these extremes by starting with budget-friendly upright compound microscope. We chose a stand and optical components that provided high quality images and designed the necessary components to motorize the z-axis of the stage. On the software side, we created a Graphical User Interface-based software to control the motorized components, drive a robust image-analysis based autofocusing system, and manage the concurrent collection of time-lapse images for multiple microscopes.

Hardware

To motorize the z-axis of the microscope, we connected the fine focus knob of the microscope to a widely available stepper motor. We designed and 3D printed a scaffold to be bolted onto the body of the microscope, providing a stable frame for the motor. A 3D printed coupler was used

to join the stepper motor and fine focus shafts (Figure 2.2). The motor is controlled by our software through an Arduino and microcontroller card (Figure 2.3). All components of the motorization, including the 3D printer and necessary hardware tools can be purchased through online retailers. Total cost of materials is less than $200 for the first motorized microscope. Motorization of additional microscopes is less than $30 per microscope, as initial materials including Arduino, 3D printing plastic, solder, etc. can used for multiple microscopes. Components can be assembled in less than one hour.

Software

To integrate control of our newly motorized microscope with time-lapse image collection, we created an intuitive GUI-based software. The open-source program offers simple mouse-based control of camera settings including exposure, frame rate, and resolution and provides live, zoom-able on-screen viewing of the sample image. It can also simultaneously manage the image data streams for multiple connected microscope cameras for concurrent time-lapse image collection. We have connected nine microscopes without issue but have not attempted more. To maintain image quality over a long-term multi-day experiment, the software implements a simple but robust image-based autofocusing program. Briefly, we determine the sharpness of the image using the variance of the Laplacian. To find the direction of adjustment necessary, initial increasingly large steps are taken until the sharpness increases beyond a predefined minimum threshold. Both directions are sampled if necessary. Then the motor takes small steps in the correct direction until the sharpness passes a local maximum. While the method cannot correct

arbitrarily large deviations from the optimal focal plane, it has shown itself to be sufficient for our purpose (Figure 2.4).

2.4 RESULTS AND CONCLUSIONS

To assess the utility of this low-budget microfluidic lifespan system, we captured whole-lifespan time-lapses of wild-type mother cells (See supplementary materials). After scoring divisions by eye, we compare the results to data collected via manual microdissection and find comparable results (Figure 2.5).

A new family of microfluidic devices promises to spur the collection of vast amounts of yeast replicative lifespan data with significantly reduced time and effort. Currently, the most common instrumentation needed to use these devices presents a significant financial barrier to all but the most well-funded laboratories. To help democratize this new technology and increase its adoption by the greater yeast community, we have designed a simple hardware and software solution to modify existing affordable microscopes. Our designs use only affordable and easy-to-find parts and require minimal technical experience (can be assembled by undergraduate students in an afternoon). While our design goals were geared towards the greater adoption microfluidic technologies for yeast replicative lifespan assays, our design will allow for the improved collection of any type of brightfield time-lapse images. Full instructions for use and assembly, CAD design .stl files for 3D printed parts, and executable software files as well as source code are available in the supplementary and on our website at www.kaeberleinlab.org.

2.5 FIGURES AND TABLES

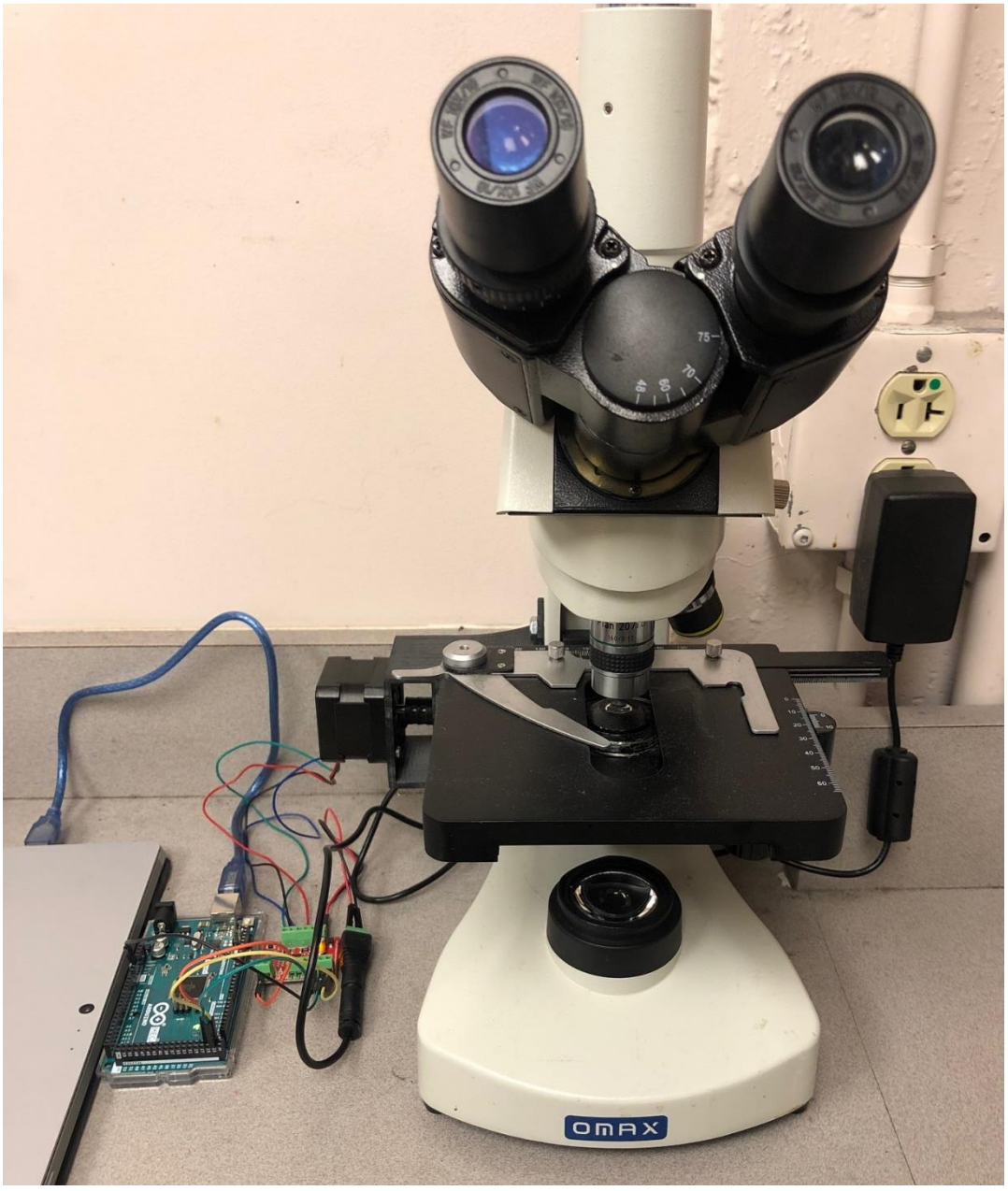

Figure 2.1. Budget light microscopy system.

Stepper motor attaches to microscope via a 3D printed scaffold, and is controlled by a computer via microcontroller chip and Arduino

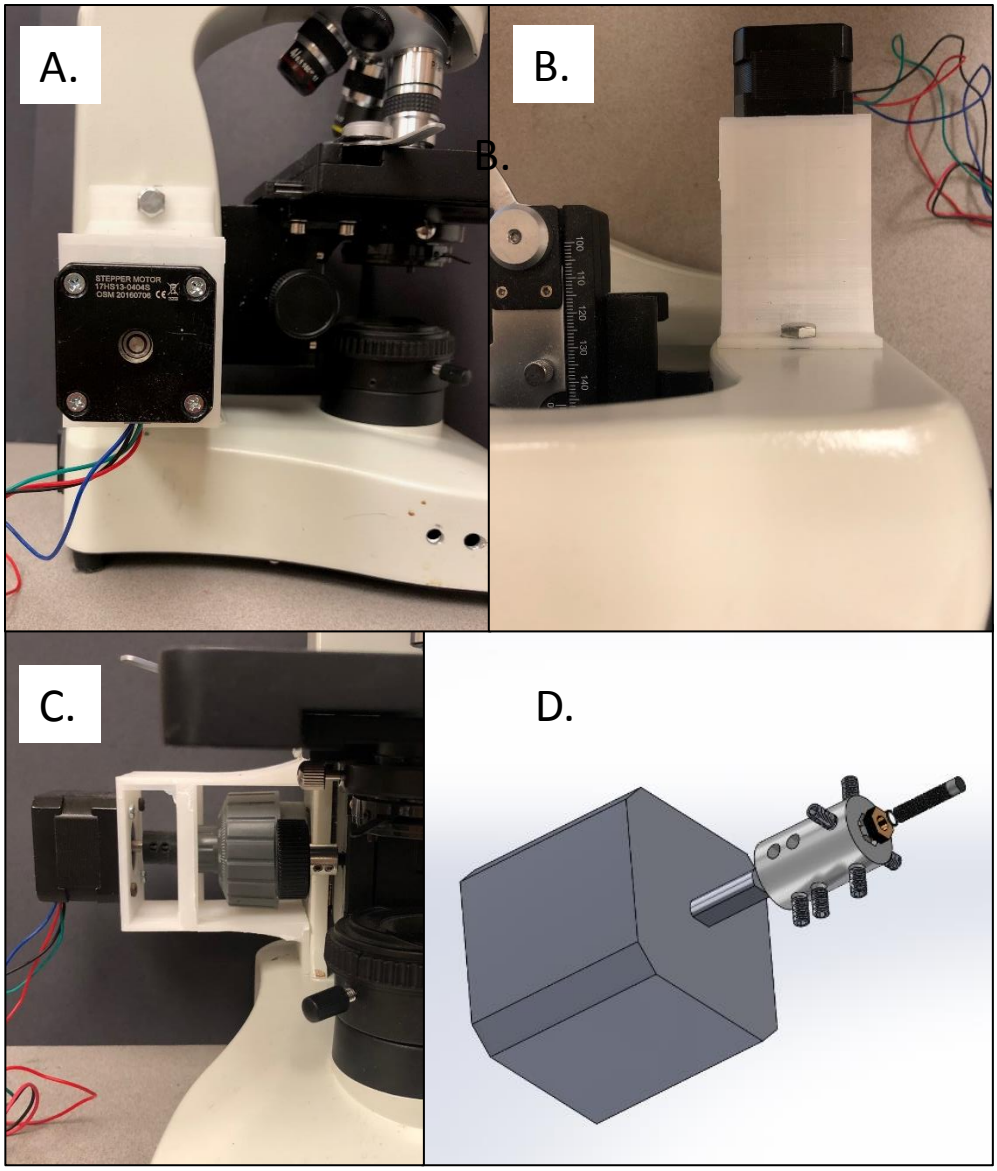

Figure 2.2. 3D printed scaffold attaching stepper motor to microscope.

A. Side view B. Top view C. Front view of motor-microscope assembly showing coupler (black cylinder) joining stepper motor shaft (silver) to fine focus (grey knob, interior shaft not visible) D. exploded view (motor, coupler, fine focus shaft from left to right) including views of optional set screws, and internal nuts and washers

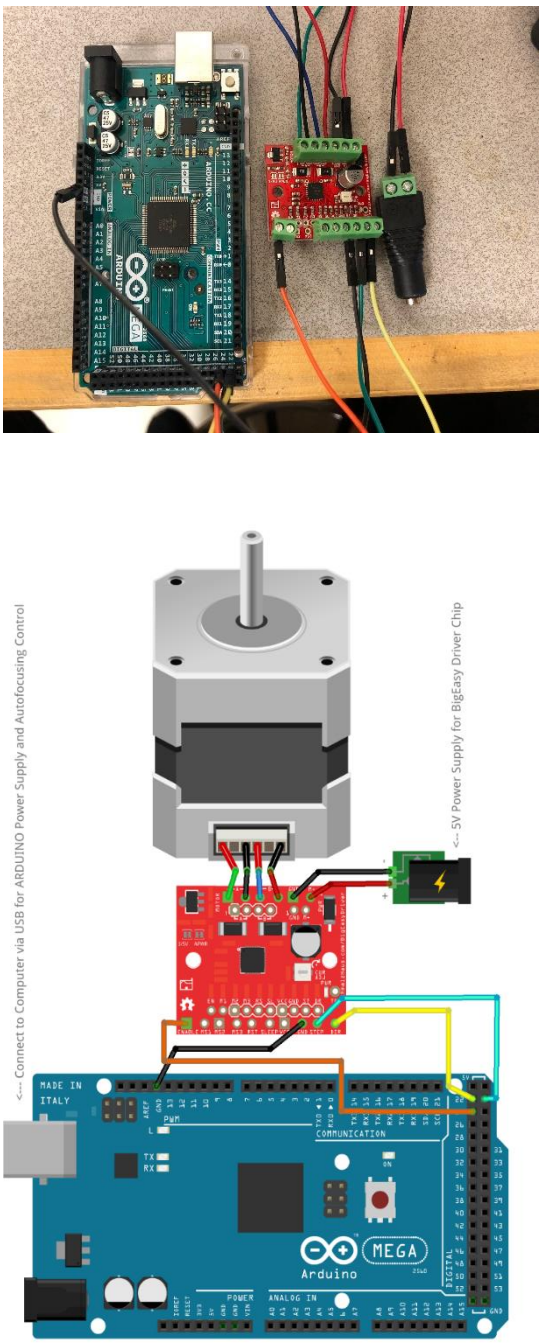

Figure 2.3. Circuitry driving stepper motor for motorized stage control

Circuit diagram showing wiring of stepper motor through BigEasyDriver controller chip and Arduino. Power supply is a 12 V DC adapter that can be plugged into a lab or household power

outlet. Arduino is connected to computer via USB. Photo of circuit diagram connections between BigEasy Driver and Arduino

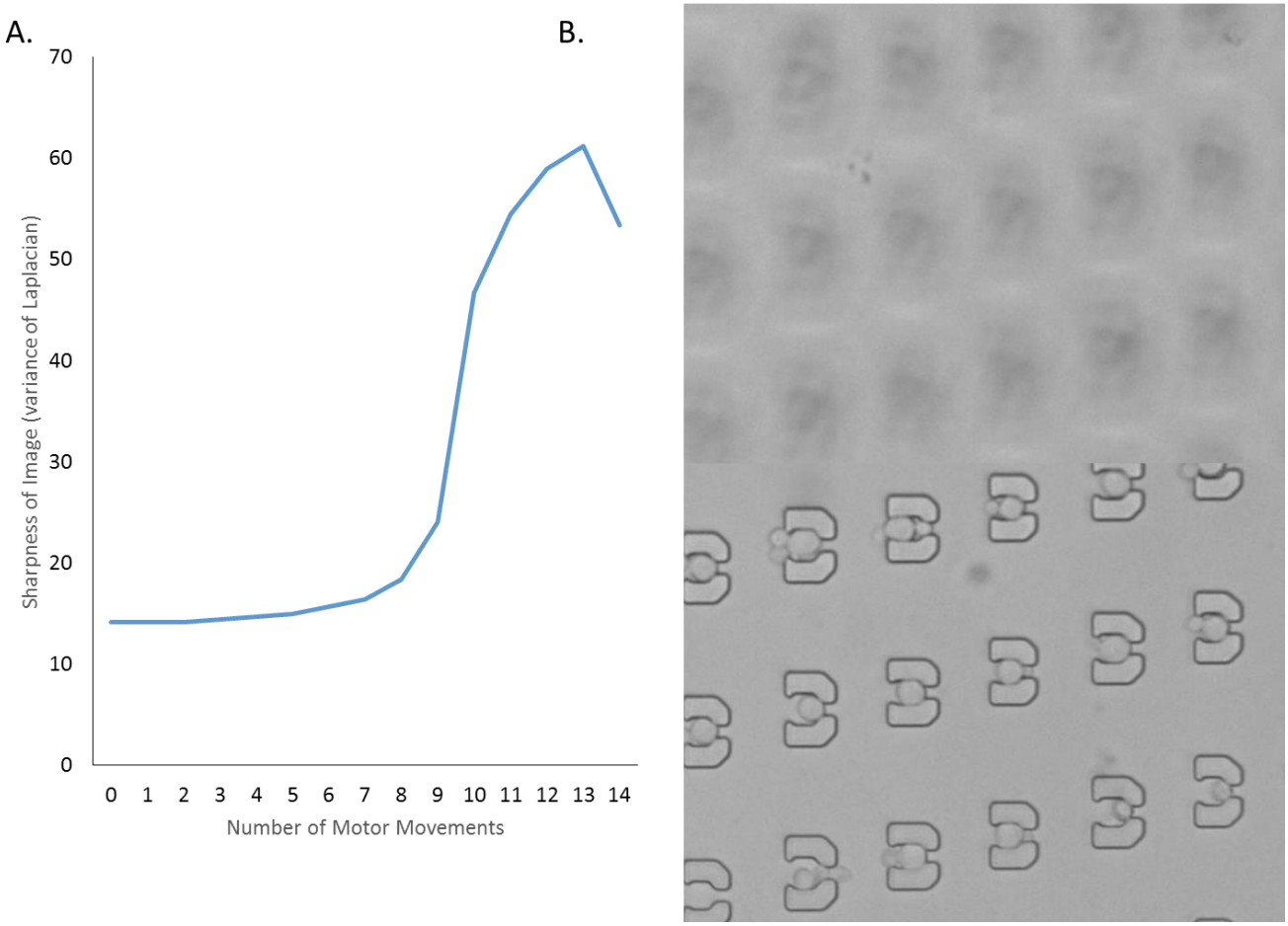

Figure 2.4. Typical autofocus performance

A. Trace of sharpness score of the live image as autofocus algorithm proceeds B. Cropped view of starting (top) and ending (bottom) images through autofocus algorithm

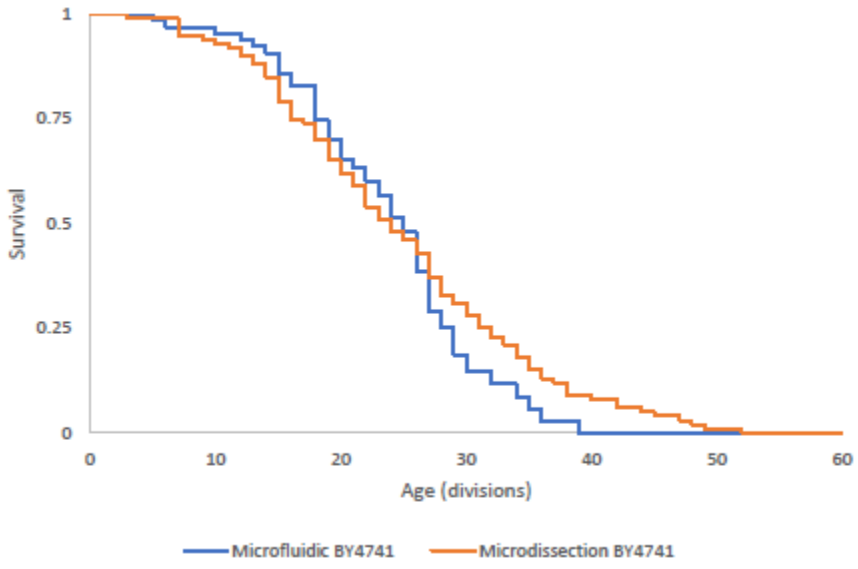

Figure 2.5. Comparison of microfluidic and microdissection lifespans

Chapter 3. DIVERGENT IRON METABOLISM AGING TRAJECTORIES

This chapter is adapted from a manuscript in preparation

Chen K., Crane, M. C., *et al.*,, Kaeberlein, M. K. Divergent iron metabolism trajectories during aging

3.1 ABSTRACT

The loss of vacuolar/lysosomal acidity is an early initiator of homeostatic decline during aging. Here, we use yeast genetics, microfluidics, and single-cell imaging to investigate the connections between vacuolar acidity, iron homeostasis, and genome instability during aging. We find that, akin to vacuolar ATPase (vma) mutants—which are unable to acidify the vacuole—aged cells suffer from genome instability and iron sulfur cluster insufficiency. However, only a subset of an isogenic, environmentally homogenous population activates the expected iron regulon against this deficiency, resulting in two divergent trajectories of iron homeostasis during aging. Iron sulfur clusters are essential cofactors for DNA polymerases and many DNA repair proteins, and we find that the iron regulon-active trajectory is characterized by extended passage and survival through a genome unstable state during aging.

3.2 INTRODUCTION

Aging is a complex process that plays an important role in disease. Study of replicative aging in the budding yeast has revealed a multitude of insights into evolutionarily conserved mechanisms of eukaryotic aging [2]. Traditionally, these studies have used a combination of genetic perturbation and bulk aged-cell enrichment techniques to capture population-level snapshots of aging physiology [3]. However, the basic shape of a survival curve informs us that even among an isogenic population—grown in a homogeneous environment—cellular lifespans show tremendous variability. Single-cell studies of both metazoan aging and budding yeast aging have shown that each cell undergoes a unique trajectory in physiological decline from birth to death [41,56,57]. However, population-level observations have been unable to fully reveal the kinetics and characteristics of these aging paths. Recent developments in microfluidic technology have

enabled researchers to characterize dynamic changes in cellular physiology at single-cell resolution [6,9–11,19,41,58]. Here, we use a combination of yeast genetics, microfluidics, and fluorescence microscopy to investigate the interplay between the loss of vacuolar acidity, iron homeostasis, and genomic instability during aging at single-cell resolution.

3.3 RESULTS

Aging is characterized by a highly penetrant but heterogeneous loss of vacuolar acidity associated with lifespan limitation

The lysosome/vacuole is a central node of cellular metabolism, with critical roles in nutrient sensing and storage, metal homeostasis, organelle maintenance, and protein degradation [59]. Accordingly, lysosomal dysfunction underlies many clinically significant genetic and degenerative diseases [60,61]. Moreover, recent studies have identified the loss of lysosomal/vacuolar acidity as an evolutionarily conserved early life driver of mitochondrial dysfunction and age-related pathology [26,38,62]. To characterize the loss of vacuolar acidity during replicative aging, we tagged the vacuolar-localized carboxypeptidase Prc1 [63] with a ratiometric pH-sensitive fluorescent protein pHluorin2 (Figure 3.7) [64]. We aged these cells in a microfluidic device with live cell fluorescence imaging saw a loss of vacuolar acidity that begins essentially at the start of life (Figure 1.1A). Using genetic perturbation, previous studies have indicated that loss of vacuolar acidity limits lifespan [26,38]. To determine whether this holds true in an isogenic, population, we found the average rate of vacuolar acidity loss during early life (ages 0-12 divisions) for each cell. In concordance with those observations, we see that the cells which

experience a faster rate of vacuolar acidity loss also ultimately have a shorter lifespan (Figure 3.1B, Table 3.4), indicating that loss of vacuolar acidity is a robust predictor of replicative lifespan within an isogenic population.

Loss of vacuolar acidity results in iron sulfur cluster insufficiency

The vacuolar ATPase is a multi-subunit protein complex which maintains the acidic environment of the lysosomal/vacuolar lumen. In mammals, genetic ablation the vacuolar ATPase function is lethal [65]. However, in the budding yeast, deletion of vacuolar ATPase subunits or assembly factors (*vma* mutants) is tolerated but results in a variety of physiological dysfunctions (in addition to alkalinization of the vacuole) including calcium sensitivity, alkaline sensitivity, iron depletion sensitivity, slow growth, sensitivity to DNA damage, reduced replicative lifespan, and respiratory incompetence [5,59,66,67]. These observations suggest that *vma* mutant cells may be a good model for aged cells, and direct study of *vma* mutants may reveal important insights into aging.

Previous investigators suggested that the loss of vacuolar acidity limits lifespan through mitochondrial dysfunction [26]. Because of this, we performed a multi-copy screen for suppressors of the *vma* respiratory deficiency phenotype. Out of ~10,000 clones, we found that overexpression of the low-affinity iron transporter FET4 allowed *vma21* knockout cells to grow under respiratory conditions. This observation concords with previous reports and our own observations that the *vma* cells display a robust activation of the iron regulon (IR) (Fig 1B) [66]. The iron regulon is a coordinated gene expression program that is activated in iron deficient

conditions that induces increased iron uptake and redistributed iron usage [68]. Interestingly, this program is triggered not by low total iron levels in the cell, but by reduced iron sulfur cluster availability [69]. Iron sulfur clusters are ancient protein prosthetic groups used in a variety of essential cellular processes including DNA replication and repair, amino acid production, protein translation, and the electron transport chain [70]. Mutations in proteins that utilize or assemble iron sulfur clusters underlie a plethora of devastating genetic cancer syndromes, hematopoietic abnormalities, and neurological diseases [70]. Iron sulfur cluster production is dependent on a series of mitochondrial iron-transfer steps [70], and it has been speculated that they are the ultimate reason for the of persistence mitochondria in anaerobic eukaryotes. Accordingly, we replicated previous findings that enzymatic activity of aconitase (a representative mitochondrial iron sulfur cluster protein) was lower in *vma21* cells than in wild-type (Figure 3.2B) [66]. Furthermore, iron supplementation suppressed the upregulated iron starvation response and rescued a variety of pleiotropic defects in *vma21* cells including respiratory deficiency, calcium sensitivity, manganese sensitivity, and sensitivity to oxidative stress (Figure 3.2D). Taken together, these observations suggest that iron dyshomeostasis, and specifically, a deficiency in iron sulfur clusters may fundamentally underlie the "unhealthiness" of *vma* mutant cells. Moreover, these observations predict that aging may be accompanied by iron sulfur cluster insufficiency.

Loss of vacuolar acidity during aging is coupled to a partially penetrant iron starvation response

Our genetic results suggested that aged cells may experience a similar deficiency in iron sulfur clusters. To test this hypothesis we created a strain with C-terminal fluorescent protein tags for

both vacuolar acidity (Prc1-pHluorin2) and an iron regulon reporter gene (Fit2-mRuby2) [66]. We found a population level activation and progressive increase in iron regulon activity during replicative aging (Figure 3.3A). On a single cell division level this iron starvation response was also associated with decreased vacuolar acidity even when controlled for age (Figure 3.3B, Table 3.5). However, we also made countless observations of aged cells with reduced vacuolar acidity but little to no activation of the iron regulon (Figure 3.3B). Indeed, many cells failed to activate the iron regulon any appreciable degree during aging (Figure 3.3C). Thus, population-level IR activation during aging was driven by a subset of cells that that generated Fit2 levels that were up to several orders of magnitude above IR inactive cells.

Divergent iron metabolism trajectories emerge during aging: active iron regulon/limited ISC deficiency and inactive iron regulon/runaway ISC deficiency

Upon observing that the age-associated iron starvation response was only partially penetrant, we were naturally curious about the single-cell levels of iron sulfur cluster deficiency during aging. Does the generation of a strong iron starvation response during aging indicate a more severe deficiency in iron sulfur clusters or vice versa?

To answer this question, we measured the activity of the essential iron sulfur cluster protein Rli1 during aging. Rli1 transports the small ribosomal subunit protein Rps2 out of the nucleus and into the cytoplasm [71]. Under conditions of iron sulfur cluster deficiency, Rps2 in accumulates in the nucleus, so that the fraction Rps2 localized to the nucleus is a measure of the insufficiency of active Rli1 and of iron sulfur clusters generally [71]. We created a reporter strain with both an iron

regulon reporter (Fit2-mRuby2) and a GFP-tagged Rps2 expressed under the GPD promoter on chromosome I. In this strain, iron sulfur cluster insufficiency results in the appearance of a bright fluorescent dot representing Rps2-GFP sequestered in the nucleus (Figure 3.4E) [71]. By observing this strain during aging in a microfluidic device, we found an overall increase in the level of iron sulfur cluster insufficiency during aging (Figure 3.4A). Unexpectedly, we saw that in middle aged and old cells (>12 divisions), severity of ISC deficiency was inversely correlated to the level of iron regulon activation (Figure 3.4B). We assigned each cell into one of two groups—iron regulon active or iron regulon inactive—based on its maximum observed Fit2 level during aging. When we measured the overall progression of ISC deficiency during aging in the IR active and inactive subpopulations, we found the ISC deficiency increased relatively equally for both groups until roughly division 12. Afterwards, as cells entered middle age, the IR-active cells plateaued in ISC deficiency during aging. IR-inactive cells, however, continued to become progressively more ISC deficient during aging (Figure 3.4C). Thus, cells could follow either IR-active/ISC-sufficient or IR-inactive/ISC-deficient aging trajectory. By visualizing the paths of all individual cells until death, we could observe that Iron regulon activation and ISC deficiency defined divergent iron homeostasis trajectories during aging (Figure 3.4D, E).

Loss of vacuolar acidity during aging is associated with increased genomic instability

Genomic instability is an evolutionarily conserved hallmark of aging. Accordingly, replicatively aged yeast show evidence of increased instability at the rDNA locus and increased incidence of genome-wide double strand breaks [72–74]. Ribosomal DNA instability and loss of homologous recombination factors during aging have been found to contribute to this instability [72,73].

However, there is not yet an overarching theory of genome instability during replicative aging. Genome maintenance is impaired during conditions of iron sulfur cluster deficiency [27,75,76]. Since vacuolar acidity is essential for iron sulfur cluster sufficiency, the loss of vacuolar acidity may be also be upstream driver of genome instability during aging. To investigate this hypothesis, we studied the development of genome instability during replicative aging in a microfluidic device using a strain with our Prc1-pH2 vacuolar acidity reporter and an mCherry-tagged Rad52, a central mediator of the DNA damage response (DDR). Rad52 is a well-known reporter of DNA damage [77]. Upon DNA double strand break, Rad52 directs the formation of gigadalton-sized protein complexes, processing centers for DNA repair through homologous recombination [78]. When Rad52 is fluorescently tagged, these DNA repair centers are visible as distinct subcellular foci [79]. Thus the appearance of Rad52 foci has been commonly used a reporter for DNA damage [77,80].

We and other researchers [80] saw a population-wide increase in the frequency of activation of Rad52-mediated DNA repair during aging, indicating a general increase in spontaneous DNA damage. As might be expected, we saw that cells which experience spontaneous DNA damage earlier in life also had shorter replicative lifespan (Table 3.6), suggesting that DNA damage may be one physiological factor that limits life. We also saw an age-controlled correlation between lower vacuolar acidity and DNA damage during aging. When looking at both activation of the DNA damage response pathway and vacuolar acidity, we saw that during middle to old-age, cells for in which the DNA damage response was activated had lower vacuolar acidity (Fig 5B). Furthermore, a faster initial drop in vacuolar acidity during early life was correlated with earlier

appearance of DNA damage during aging (Fig 5C). This is consistent with the idea that the age-associated loss of vacuolar acidity may be an upstream driver of genome instability during aging.

The iron homeostasis trajectory of a cell is associated with its genome stability behavior

Iron metabolism and genome maintenance are deeply intertwined, as iron sulfur clusters are necessary for both DNA replication and many types of DNA repair [81]. Accordingly, iron deficiency potentiates sensitivity to DNA damage and impairment of iron sulfur cluster production has been shown cause genome instability [27]. Because of this, we were curious about any differences in genome stability between cells from divergent iron metabolism aging trajectories. We created strains with both an iron regulon reporter (Fit2-mRuby2) and a DNA damage reporter (Rad52-GFP) and observed their replicative aging in a microfluidic device. We broadly separated our cells into two groups, either iron regulon-active or iron regulon-inactive based on the maximum iron regulon activity observed during aging. We saw that the cells which activated the iron regulon during aging survived for longer after initial observation of spontaneous DNA damage (Fig 6B). Iron regulon active cells also underwent more cell divisions during which the DNA damage response had been activated (Fig 6C). This suggests that because the IR-active cells experienced limited ISC deficiency during aging, they were likely better survive spontaneous age-related DNA damage by marshalling the appropriate ISC-dependent DNA repair processes.

Interestingly we saw differing relationships between DDR activation and longevity between these two iron metabolism groups. Within the IR-active group, longer lifespan was correlated with additional divisions during which the DNA damage response was activated (Fig 6D).

Within the IR-inactive group, there was no correlation between longer lifespan and activation of the DNA damage response (Fig 6D). Taken together these suggest that the longest-lived cells within these groups may have different molecular processes underlying their success. Within the IR-active group, longevity may be determined by the robustness of the repair and survival responses to spontaneous DNA damage. Within the IR-inactive group, with more severe ISC deficiency and potentially less capability to repair DNA damage, longevity may be correlated to minimal spontaneous DNA damage during aging.

3.4 DISCUSSION

Recent developments in microfluidic device technology have opened the ability to characterize replicative aging with whole-lifespan breadth and single-cell resolution. Using a combination of microfluidics, fluorescence microscopy, and traditional yeast genetics, we have a further characterized the consequences of the loss of vacuolar acidity, an early-life physiological change during aging. Using an overexpression screen for suppressors of *vma* mitochondrial dysfunction, we found that loss of vacuolar acidity results in iron sulfur cluster deficiency, and iron dyshomeostasis underlies many of the "sick" phenotypes of *vma* mutant cells. Showing that *vma* deletion are a valuable model for aging, we found that aged cells also display both a deficiency in iron sulfur clusters and an increase in genome instability. Furthermore, both of these physiological declines correlate with vacuolar acidity loss when controlled for age, suggesting that vacuolar dysfunction may play a role in age-associated increase in genomic instability. Iron sulfur cluster proteins function in a wide variety of physiological contexts and are highly conserved evolutionarily [81]. Moreover, defects in iron sulfur cluster production or in specific iron

sulfur clusters underlie numerous genetic syndromes with progeroid characteristics as well as many age-associated diseases [61]. The loss of vacuolar acidity is an evolutionarily conserved aging phenotype, and impairment of lysosomal acidity has been tied to iron dyshomeostasis in mammalian cells [82]. Because of this, we postulate that the depletion of iron sulfur clusters with age may be a fundamental and evolutionarily conserved driver of clinically significant age-associated pathology.

Interestingly, only a subset of cells can activate the expected iron regulon program in response to iron sulfur cluster deficiency during aging. Thus, an isogenic, environmentally homogeneous population of yeast cells follows divergent iron metabolism trajectories during aging. IR-active cells mount a robust iron starvation response, resulting in limited iron sulfur cluster deficiency throughout life. In contrast, more than half of the population is unable to mount any meaningful IR activity, resulting in a progressive increase in iron sulfur cluster deficiency during aging. This divergence has implications on other measures of physiology during aging, including cellular responses to age-associated spontaneous DNA damage. We find that in general, IR active cells are better able to survive and continue dividing during episodes of DNA damage, with a strong correlation between longer lifespan and additional DNA damage episodes survived. In contrast, IR-inactive cells seem particularly sensitive to DNA damage, and longer-lived cells in this population appear to be those which required minimal activation of the DNA damage response. Notably, we have not attempted to fully characterize the differences between the IR-active and IR-inactive subpopulations, including the mechanistic details of DNA damage survival during aging. It is unknown whether surviving cells are repairing this damage using high or low-fidelity mechanisms or if they are undergoing adaptation resulting in further division.

The cell-state divergence during aging that we describe has previously characterized in terms of mother and daughter cell morphology by Jin, et al. 2019 [45]. Although no gene expression or mechanistic observations were made in that study, our shared observations suggest that the aging process may have characteristics reminiscent of Waddington's landscape of development, where cells diverge into distinct aged states. These trajectories may be more fully characterized by single-cell observation of additional gene expression or physiological parameters. While this study and Jin, et al. did not make observations of any shared parameters, it is likely that integration of these observations as well as those of other physiological variables will result in identification more divergent aging states. Ultimately, whether the total multidimensional landscape of aging can be best understood as a finite array of valleys, or whether this analogy is better suited to separate understanding of single parameters of aging is yet to be determined.

In mammalian tissue, induction of senescence produces functionally distinct senescent cell types [83]. Moreover, single-cell studies of aging mammalian tissues show that cells within a single tissue experience "fate drift" or a progressive increase in transcriptional cell-to-cell variability [84,85]. Interestingly, some types of dysplastic transformation are associated with passage through particular transcriptional trajectories [86]. This raises the possibility that oncogenic transformation during aging may have some dependence on transcriptional state in addition to the classically understood mutational pathways. Interestingly, both iron overload and deficiency of iron sulfur cluster-dependent processes have been implicated in carcinogenesis, and cancer stem cells have been associated with characteristic iron metabolism transcriptional profiles [87,88]. We see that cells can follow divergent iron metabolism trajectories during replicative aging, which correlate with

differing genome instability behavior. In mammalian tissue, little is known about the whether gene-expression diversity within a tissue may potentiate oncogenic mutagenesis in certain cells. Whether there exist iron metabolism states that confer higher oncogenic potential onto certain cells with during aging is an open question that should be explored in the future.

3.5 MATERIALS AND METHODS

Reagents.

Yeast strains used in this study are haploid and derived from the BY4741/4742 (S288C derived) background. Genotypes are shown in supplemental table 3.

Ammonium iron (II) sulfate hexahydrate (Sigma) was used at 0.5 – 2.5 mM.

Yeast suppression screens

The multicopy suppression screen was performed using a YEP13 library (2μ, LEU2 vector) containing 5-20kb inserts of yeast genomic DNA [89]. The YEP13 pooled library was transformed into vma21 and vma13 vma21 double mutants and plated onto media lacking leucine to select for plasmid transformation. ~10,000 colonies were then replica plated onto YEP + glycerol media. For colonies that grew, the plasmid was isolated from yeast using a Qiagen plasmid prep kit (with glass beads added to lysis buffer) and the plasmid was transformed into E.coli, isolated (Qiagen) and sequenced with primers flanking the insertion site to identify the genomic region contained on the plasmid. For validation, we cloned FET4 with ~400bp upstream promoter into the pAG425 (resulting plasmid named pBMW182a) backbone using the Yeast Gateway System Vectors (obtained from Addgene) [90].

Yeast growth assay

Yeast growth assays on solid agar containing media were performed similarly to as previously described [70] . Briefly, yeast strains were diluted into water to identical optical densities. Cells were aliquoted into 96 well microplates, five-fold serially diluted in water, and 4.5 µl of each sample was pipetted onto the indicated media type. After drying, plates were incubated at 30°C, for 2-5 days.

Aconitase activity assay

Aconitase activity was performed similar to previously described [92]. Briefly, cell extracts were incubated with 0.2mM phenazine methosulfate, 0.5mM MTT (3-(4,5-Dimethylthiazol-2-yl)-2,5-Diphenyltetrazolium Bromide), 0.25 mM NADP, 2.5 mM cis-aconitic acid, and 0.4U/ml isocitrate dehydrogenase and absorbance at 450 nm was measured. An isocitrate standard was used to generate a standard curve and experimental data was collected with absorbance values that fell within the range of the linear standard curve. BCA assay was used to add equal protein amounts from each sample.

Flow cytometry

Cells were grown to log phase in the indicated condition and cells were spun down, transferred into water, and stored on ice briefly until flow cytometry was performed with a FACSCanto II flow cytometer at the University of Washington Pathology Flow Cytometry Core Facility. Excitation was using a 488 nm laser and emission was monitored with a 502 long pass filter and

530/30 filter. Three biological replicates were measured, each of which consisted of 20,000 cells per condition.

Microfluidics and Fluorescence Microscopy

Cells were imaged using a PDMS microfluidic flow chamber with cell traps modified to increase mother cell retention and introduction of multiple chambers to isolate cells of different genotypes in identical environments. Cells were loaded according to previously published methods. A volumetric flow rate of 1-12 μL/min per chamber was used. Flow rate was initialized at low rate to prevent ejection of smaller young mother cells from traps and increased throughout the experiment to reduce cell clogging and maintain the trapping of large older mother cells. Cells were imaged using a Nikon Ti-2000 microscope with a 40X oil immersion objective, 1.3 NA using the Nikon Perfect Focus System. An enclosed incubation chamber was used to maintain a stable environment at 30 C. An LED illumination system (Excelitas 110-LED) was used to provide consistent excitation energies, with illumination triggered by camera shutter to prevent excess exposure. Images were acquired using a Hammamatsu Orca Flash 4.0 V2. Camera and stage were controlled by in-house software written in Matlab® and Micromanager. Images were corrected for illumination artifacts. To correct for single pixel biases, 1,000 images were acquired with no illumination, and individual pixel means were determined. To correct for flatness of field, fluorescent dye was added to a microfluidic device. 1,000 images were acquired each with a small offset in the x and y positions (to compensate for microfluidic trap features). Images were dilated, and the median value at each location was used. For every image, pixel-level bias was subtracted and values were multiplied by a flatness of field correction factor. Brightfield images were acquired at 5 min intervals for bright-field. Fluorescence imaging was

acquired at 30 minute or 1 hr intervals. For bright-field imaging, 3 z-sections were 3.5 µm intervals. For the fluorescence, 3-7 z-sections were acquired. GFP images were acquired using a Chroma ET49002 filter set. For, mRuby2 and mCherry images were acquired using a Chroma ET49306 filter set. For pHluorin2 ratiometric imaging, the Chroma GFP ET49002 filter set and a custom ET405/40X excitation, ET525/50m emission filter set (Chroma) were used. Following data acquisition, cells were segmented and tracked using previously published software(Bakker et al., 2017). Divisions were scored by eye, and errors in cell segmentation and tracking were corrected manually. For Fit2 mean fluorescence values of maximum projection were interpreted to reflect total protein levels. For vacuolar acidity, for each cell, the brightness of the two fluorescence channels were equalized and summed, and the brightest 5% of pixels were used. The mean of the pixel-level ratio of these channels was used as a measure of vacuolar acidity. For Rad52 foci presence, the value of the brightest 9-pixel square divided by the brightest 2.5% of the cell was used. A threshold of was determined by visual inspection of foci-containing and foci-free cells. (1.1 for GFP, 1.05 for mCherry). For Rps2 nuclear retention, the value of the brightest 9 pixel square divided by the mean brightness of the cell was used.

Cells were inoculated into SC media (Sunrise Biosciences) with 2% dextrose and grown overnight (~12-24 hours) until log phase. BSA was added to immediately prior to loading to prevent adherence to PDMS. During experiments, SC media with 2% dextrose was used, and cells were imaged for 60-80 hrs.

3.6 FIGURES AND TABLES

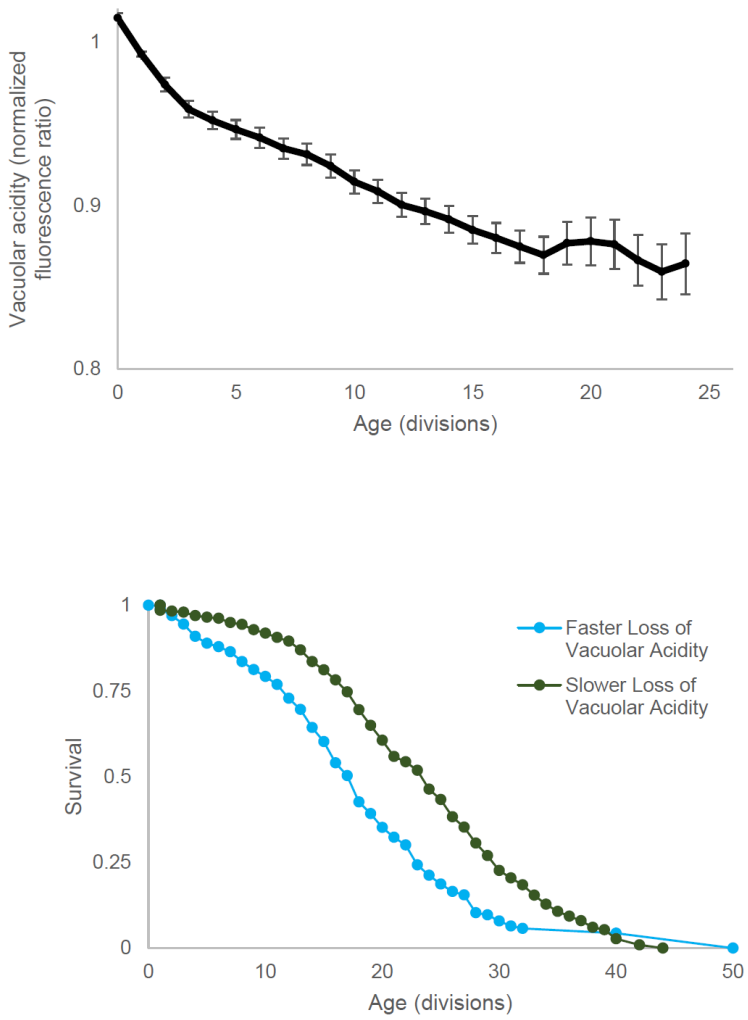

Figure 3.1. Vacuolar acidity declines during aging.

A. Vacuolar acidity trend during aging, as measured by fluorescence ratio of vacuole-localized Prc1-pHluorin2. Acidity is normalized per cell to young cell value (average before the second division). r = -0.259 , p = 1 x 10^{-149}, n = 9857 cell-divisions, error bars are SEM.

B. Survival curves for the population partitioned into two groups by the rate of vacuolar acidity loss during early life (0-12 divisions). Population is split in half using the median rate of vacuolar acidity loss. Fast rate of decline in vacuolar acidity is associated with shorter lifespan, logrank $p = 2.22 \times 10^{-16}$, n = 289 cells per group.

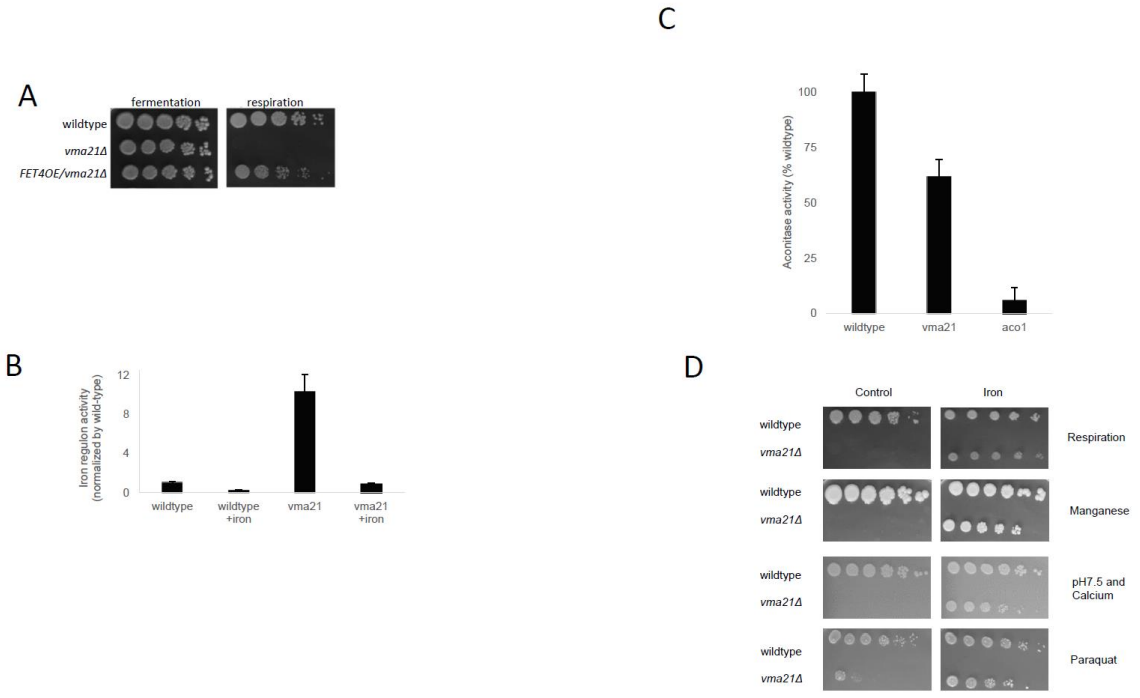

Figure 3.2. Ablation of vATPase activity causes iron dyshomeostasis

A. Overexpression of FET4 from a high copy (2μ) plasmid increases survival of *vma21* mutants under respiratory conditions.

B. Flow cytometry analysis of GFP levels under control of the iron regulon promoter (Fit2), wildtype and *vma21* mutants grown under fermentative conditions (YPD media), with or without 1 mM iron. Values are the mean of 3 samples of 20,000 cells each.

C. Iron sulfur cluster enzyme aconitase activity for wildtype, *vma21*, and *aco1* mutants. Bonferroni corrected ANOVA $p < 0.001$ for all comparisons.

D. Iron supplementation (2.5 mM iron (II) ammonium sulfate) rescues multiple "deficiencies" of *vma21* mutants including respiratory deficiency, manganese (1 mM) sensitivity, alkaline calcium (buffered to pH 7.5 and 20 mM $CaCl_2$) sensitivity, oxidative stress (1 mM paraquat) sensitivity

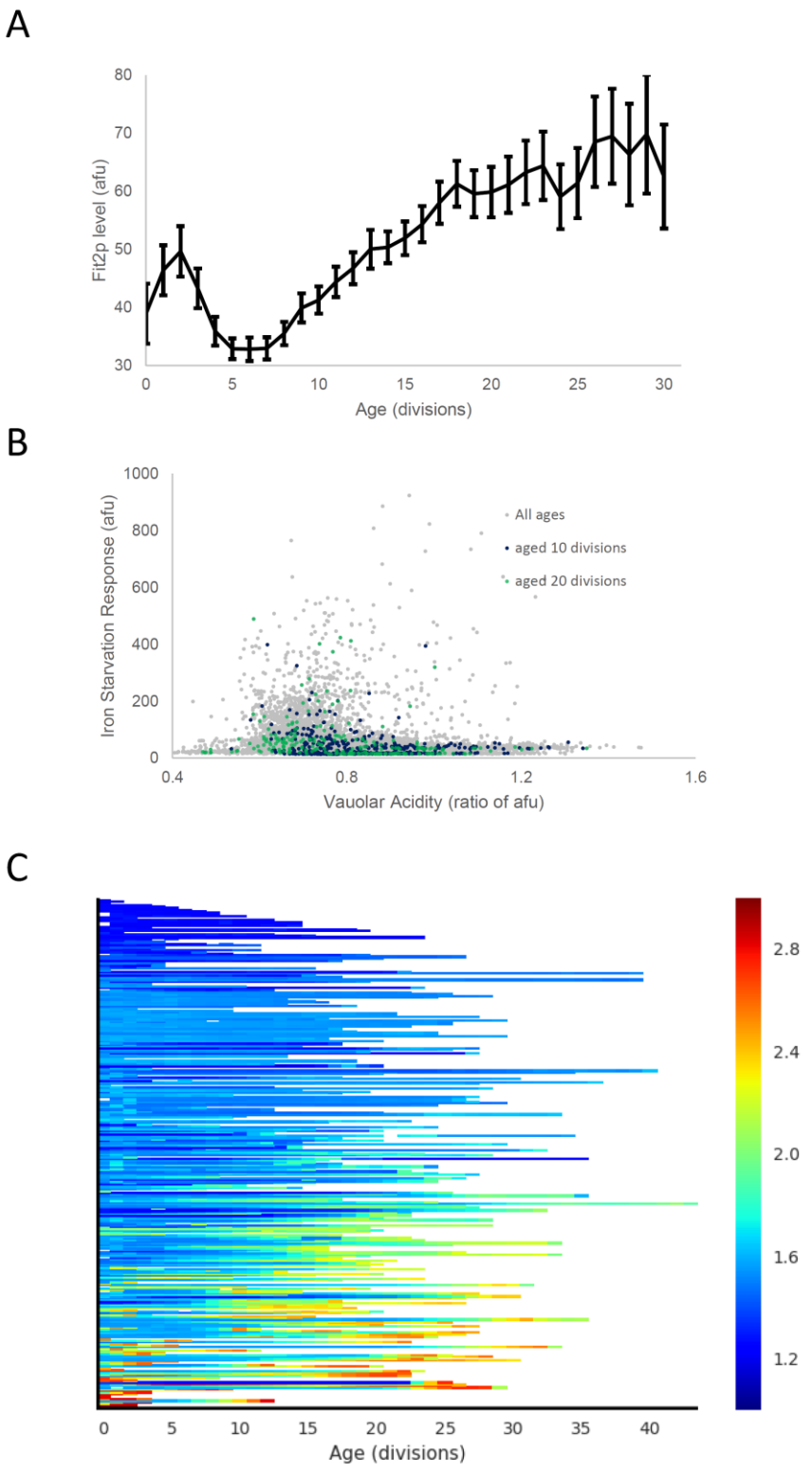

Figure 3.3. Iron regulon activity during aging

Iron regulon activity is associated with the loss of vacuolar acidity and increases with age. However, a large subset of cells show little to no iron regulon activity during aging.

A. Age associated trend of population average iron regulon activity. Iron regulon activity increases with age, Pearson $r = 0.13$, $p < 10^{-38}$
B. Scatter plot of iron regulon activity and vacuolar acidity for all cells at all ages. Iron regulon activity is correlated with lower vacuolar acidity even when controlled for age (All ages: Spearman $\rho = -0.21$, $p < 10^{-4}$; age 10: Spearman $\rho = -0.17$, $p = 0.0017$; age 20: Spearman $\rho = -0.38$, $p< 10^{-4}$)
C. Single cell lifetime trajectories of measured iron regulon activity. Color values are log(Fit2-mRuby2 fluorescence). Many cells show little to know iron regulon activation.

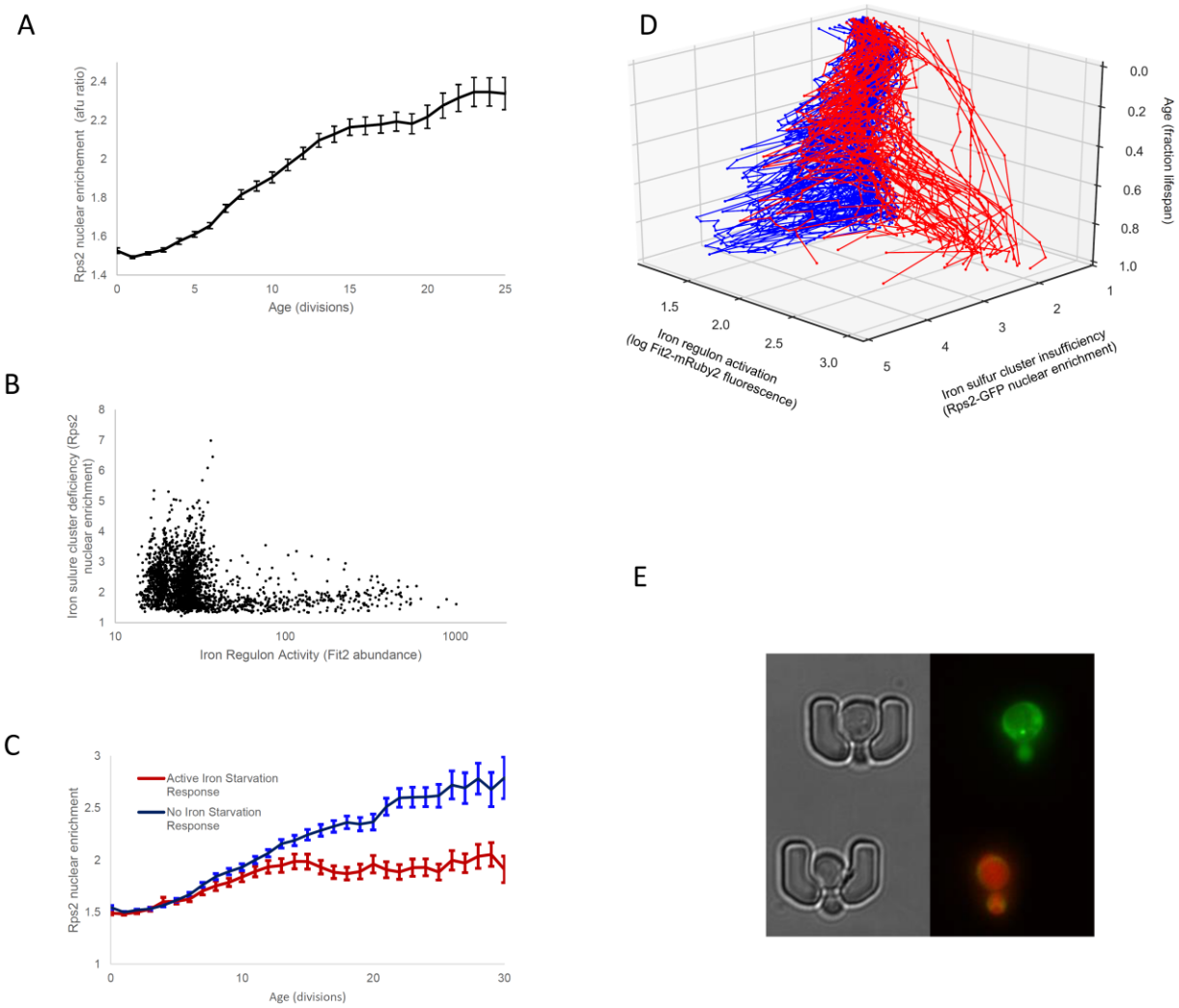

Figure 3.4. Iron regulon activation relieves iron sulfur cluster deficiency

Iron sulfur clusters become deficient during aging. Activation of iron regulon is inversely correlated with iron sulfur cluster deficiency. Cells with robust iron regulon activity during aging generally follow a trajectory of limited iron sulfur cluster deficiency.

A. Aging trend of population mean Iron sulfur cluster insufficiency (Rps2 nuclear enrichment). Iron sulfur cluster insufficiency increases during aging. Pearson $r = 0.52$, $p < 10^{-4}$.

B. Scatter plot of iron sulfur cluster insufficiency (nuclear enrichment of Rps2-GFP) and iron regulon activation (Fit2-mRuby2 fluorescence) in aged cells (all cells and ages > 12 divisions). Spearman $\rho = -0.26$, $p < 10^{-4}$.

C. Aging trend of Iron sulfur cluster deficiency for iron regulon competent and incompetent cells during aging. Iron regulon active cells are defined as having a maximum Fit2 fluorescence level that is 3x the median baseline. Iron regulon inactive cells are not more iron-starved during early life, but have less severe iron sulfur cluster deficiency from middle to old age ($p < 0.05$ for ages 15-30).

D. Single cell trajectories of iron sulfur cluster deficiency and iron regulon activity during aging. Cells display divergent iron metabolism trajectories during aging: Red: iron regulon active with limited iron sulfur cluster deficiency. Blue: no iron regulon activation

E. Example aged cells in adjacent traps from each iron metabolism trajectory. Top: Iron sulfur cluster deficiency (Rps2-GFP nuclear retention visible as bright green dot) with little iron regulon activation. Bottom: Robust iron regulon activation (Fit2-mRuby2) with no visible Rps2-GFP nuclear retention.

A

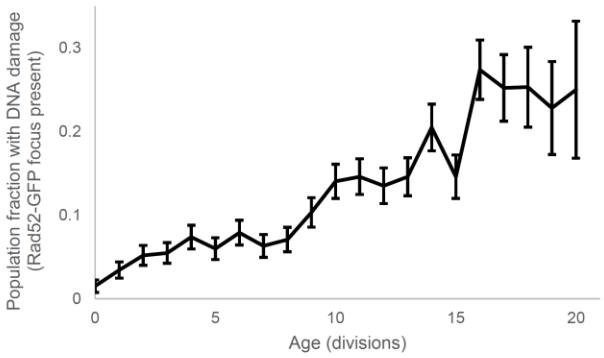

B

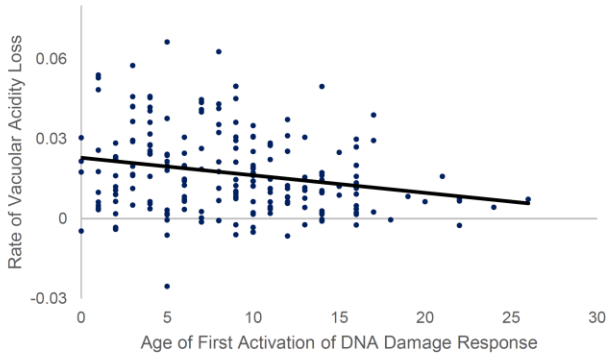

C

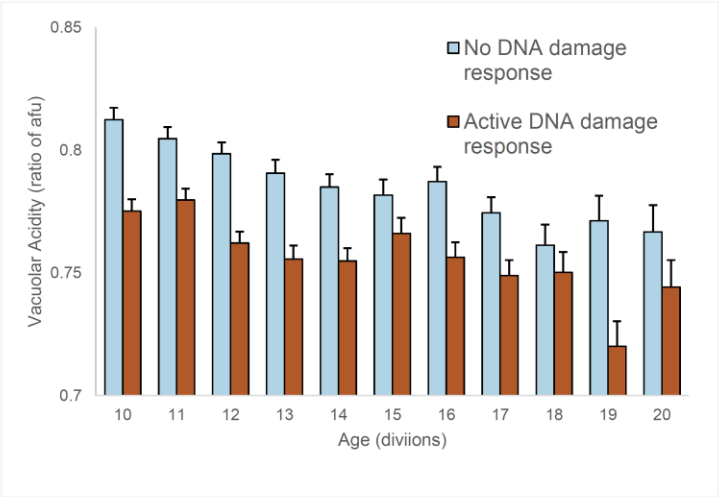

Figure 3.5. DNA damage during aging

Activation of the DNA damage response increases during aging, is correlated with the loss of vacuolar acidity, and is predictive of a shorter replicative lifespan.

A. Aging trend of DNA damage response activation as measured by presence of Rad52-GFP focus. As cells age the fraction of cells that activate the DNA damage response increases, $r = 0.27$, $p < 10^{-4}$,
B. Scatter plot of age of first DNA damage response activation (Rad52-GFP foci) and rate of vacuolar acidity loss in early life for cells which activate the DNA damage response at any point during life. (ages: 0-12 divisions Faster loss of vacuolar acidity during early life (ages 1-12 divisions) correlates with earlier appearance of DNA damage response. $r = -0.23$, $p = 0.0006$
C. Comparison of vacuolar acidity for cells with and without activated DNA damage response (Rad52-GFP foci) at various ages. Presence of activated DNA damage response (Rad52-GFP foci) is associated with lower vacuolar acidity when controlled for age. All comparisons ranksum $p< 0.05$ except for ages 15: $p = 0.089$, 18: $p = 0.45$, 20: $p = 0.20$.

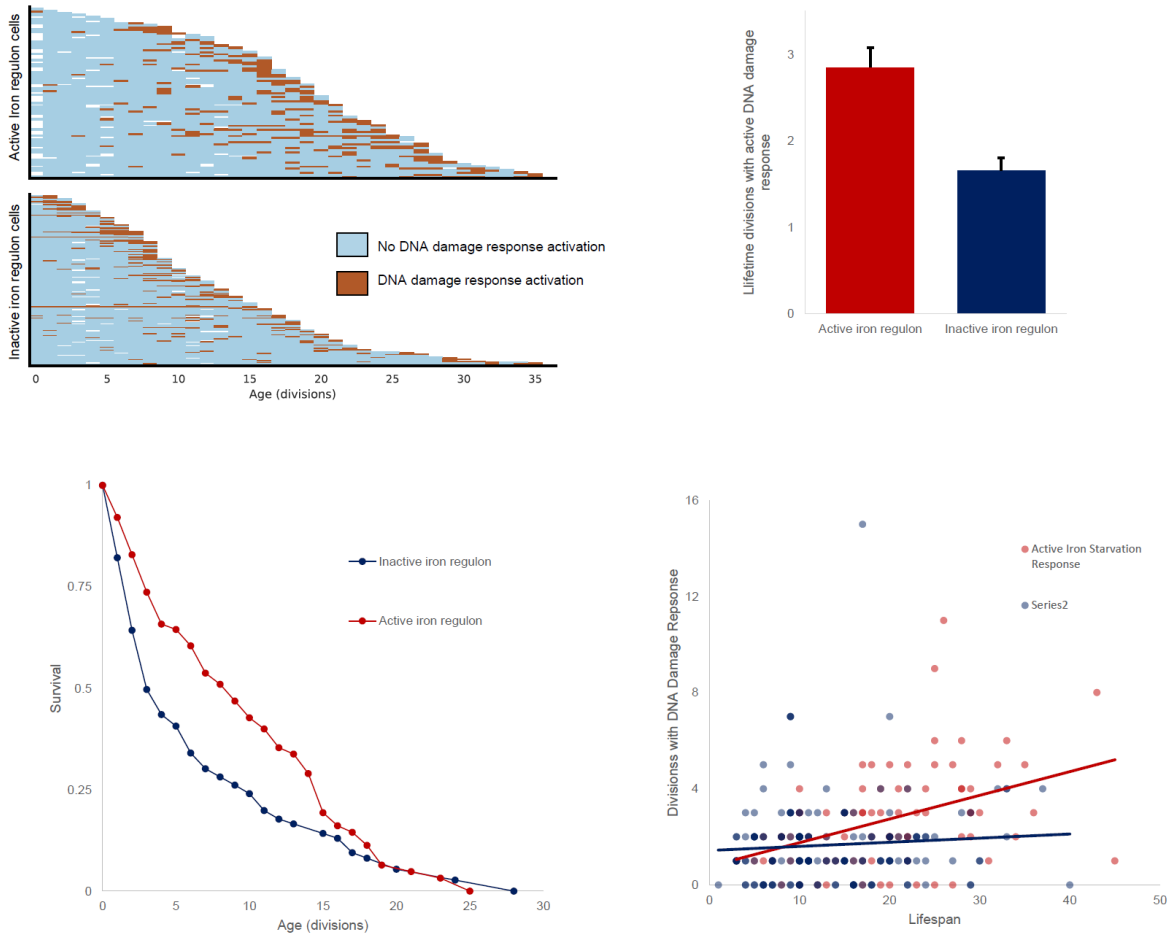

Figure 3.6. DNA damage for iron regulon active and inactive cells

Iron regulon active survive longer after the first activation of the DNA damage response during aging and undergo more lifetime divisions during which the DNA damage response (Rad52-GFP foci formation) is activated. Total lifespan of iron regulon active cells is highly correlated to the number of lifetime divisions during which the DNA damage response is activated. Within the iron regulon inactive group, longer-lived cells do not undergo any more divisions with DNA damage than shorter lived cells. This suggests that within the IR competent subpopulation, the longest-lived cells are those with the most robust ability to survive age-associated DNA damage.

Within the IR incompetent subpopulation, the longest-lived cells are those lucky with minimal age-associated DNA damage.

A. Single cell trajectories of DNA damage response activation during aging. Top: Cells that activate the iron regulon during aging (maximum lifetime Fit2-mCherry fluorescence > 3x median baseline level) Bottom: Cells that fail to activate the iron regulon during aging.
B. Survival curves comparing remaining lifespan after first observed activation of the DNA damage response (Rad52-GFP focus formation) for iron regulon competent and incompetent cells. Cells that activate the iron regulon during aging have increased survival after the first activation of the DNA damage response logrank $p = 0.018$, $n_{\text{active iron regulon}} = 76$, $n_{\text{inactive iron regulon}} = 129$.
C. Comparison of DNA damage response activation between iron regulon active and iron regulon inactive cells. During aging, cells that activate the iron regulon undergo more divisions during which the DNA damage response is activated.
D. Scatter plots showing correlation between total lifespan and number of divisions during which the DNA damage response is activated. Longer lifespan of the iron regulon active cells is well-correlated ($r = 0.41$) with a higher number of divisions with an activated DNA damage response. Longer-lifespan in iron regulon inactive cells is not correlated ($r = 0.08$) with more divisions with DNA damage. Comparison of correlation coefficients by Fisher's Z-transform $p = 0.01$.

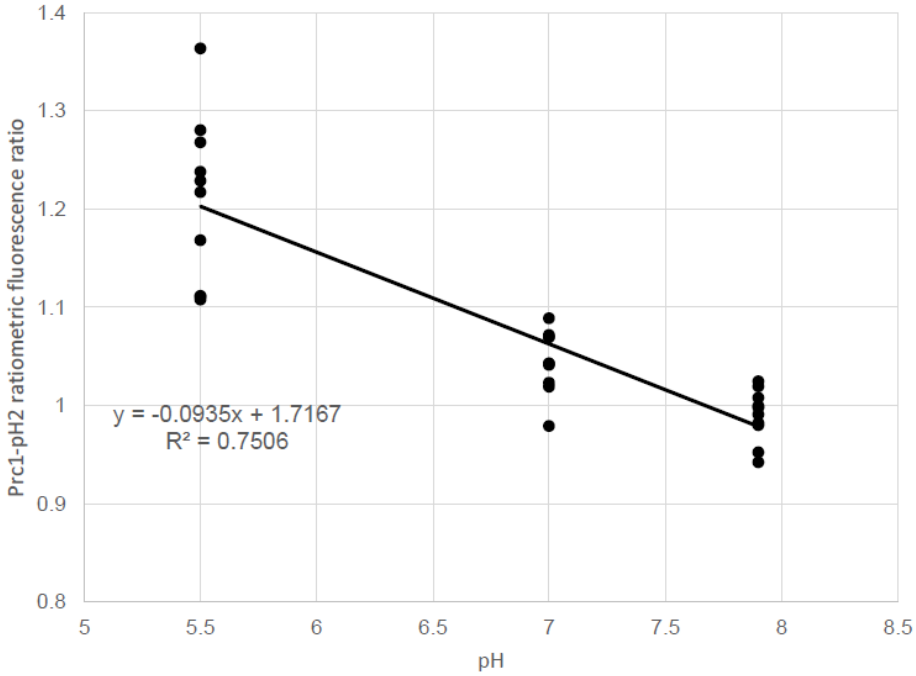

Figure 3.7. pHluorin2 fluorescence ratios

Prc1-pHluorin2 ratiometric fluorescence ratio reports the vacuolar pH. Vacuolar fluorescence ratio (Prc1-pHluorin2 ratiometric fluorescence ratio) for cells with inhibited ATPase and incubated in buffered solution

Table 3.4. Correlation between vacuolar acidity and remaining lifespan

Age	Pearson r	p
4	0.10	3.66E-04
5	0.11	1.47E-04
6	0.16	1.81E-07
7	0.17	3.46E-08
8	0.22	5.92E-13
9	0.24	4.01E-15
10	0.23	1.86E-13
11	0.26	1.57E-16
12	0.27	2.96E-16
13	0.21	1.10E-10
14	0.25	4.19E-13
15	0.23	7.90E-11
16	0.22	1.33E-09
17	0.23	4.84E-09
18	0.22	4.66E-08
19	0.21	8.24E-07
20	0.23	6.89E-07
21	0.22	7.28E-06
22	0.16	1.50E-03
23	0.19	3.02E-04
24	0.20	6.27E-04
25	0.16	1.20E-02
26	0.25	2.01E-04
27	0.22	2.10E-03
28	0.18	2.24E-02
29	0.23	8.43E-03
30	0.31	1.80E-03

Higher vacuolar acidity as measured by fluorescence ratio of Prc1-pHluorin2 is significantly correlated to higher remaining lifespan across the aging timeline. Each row shows the correlation coefficient and statistical significance between remaining lifespan and vacuolar acidity at a particular age for all cells.

Table 3.5. Correlation between vacuolar acidity and iron regulon activity

Age	Spearman rho	P value
10	**-0.16**	**1.49E-03**
11	**-0.19**	**2.20E-04**
12	**-0.22**	**4.38E-05**
13	**-0.24**	**6.42E-06**
14	**-0.29**	**7.90E-08**
15	**-0.32**	**8.74E-09**
16	**-0.39**	**1.31E-12**
17	**-0.35**	**3.07E-10**
18	**-0.35**	**3.04E-09**
19	**-0.37**	**1.31E-09**
20	**-0.38**	**4.86E-10**
21	**-0.36**	**9.74E-09**
22	**-0.36**	**6.27E-08**
23	**-0.34**	**7.81E-07**
24	**-0.35**	**2.28E-06**
25	**-0.30**	**1.76E-04**

Correlation between vacuolar acidity (Prc1-pH2 fluorescence ratio) and iron regulon activity (Fit2-mRuby2 fluorescence). When controlled for age, vacuolar acidity and iron regulon activity are inversely correlated.

Table 3.6. Correlation between DNA damage response and lifespan

Age	Hazard Ratio	p
1	**1.688**	**0.091**
2	**1.387**	**0.173**
3	**1.513**	**0.044**
4	**1.591**	**0.009**
5	**1.575**	**0.006**
6	**1.591**	**0.003**
7	**1.571**	**0.003**
8	**1.558**	**0.003**
9	**1.540**	**0.002**
10	**1.364**	**0.025**
11	**1.335**	**0.034**
12	**1.278**	**0.069**

Activation of the DNA damage response (measured by presence of Rad52-GFP foci) in early life is associated with shorter lifespan. Table shows the cox proportional hazards ratio for cells with early activation of the DNA damage response v cells with no early activation of the DNA damage response. Early activation is defined as activation of the DNA by the age shown in the first column.

Table 3.7. Strains used

Strain	Background	Genotype	Reference/Source
BY4741	BY4741	Wildtype, MATa ura3Δ his3Δ1 leu2Δ met15Δ	Thermo
BY4742	BY4742	Wildtype, MATα ura3Δ his3Δ1 leu2Δ lys2Δ	Thermo
BW1016	BY4742	vma21::URA3 his3Δ1 leu2Δ lys2Δ	this study
BW1017	BY4741	vma21::URA3 his3Δ1 leu2Δ met15Δ	this study
BW1008	BY4741	FIT2pr::GFP	Diab, H. I. & Kane, P. M.. J Biol Chem (2013).
BW1025	BW1008	FIT2pr::GFP vma21::URA3	this study
KC385	BY4742	prc1::Prc1-pHluorin2, HphNT1 fit2::Fit2-mRuby2, CaHis5	this study
KC620	BY4742	pGPD::Rps2-GFP, URA3 fit2::Fit2-mRuby2 CaHis5	this study
KC631	BY4741	prc1::Prc1-pHluorin2, HphNT1 rad52::Rad52-mCh, KanMX	this study
KC614	BY4741	fit2::Fit2-mCherry, KanMX rad52::Rad52-GFP, HIS	this study, generated from yeast GFP collection

Chapter 4. CONCLUSION

In this work, we extend the applicability of microfluidic devices to the study of yeast replicative aging by developing a low-cost motorized microscopy system. We hope that this facilitates the wider adoption of microfluidic device technology for yeast aging experiments. We use a microfluidic device to investigate open questions on the mechanisms linking vacuolar acidity, iron metabolism and genome stability during aging. We find an interesting phenomenon of divergent single-cell trajectories of iron metabolism during aging, we different age-associated behavior in genome stability and survival during DNA damage.

BIBLIOGRAPHY

1. Mortimer, R. K. & Johnston, J. R. Life Span of Individual Yeast Cells. *Nature* **183**, 1751–1752 (1959).
2. Wasko, B. M. & Kaeberlein, M. Yeast replicative aging: a paradigm for defining conserved longevity interventions. *FEMS Yeast Research* **14**, 148–159 (2014).
3. Lippuner, A. D., Julou, T. & Barral, Y. Budding yeast as a model organism to study the effects of age. *FEMS Microbiology Reviews* **38**, 300–325 (2014).
4. Steffen, K. K., Kennedy, B. K. & Kaeberlein, M. Measuring Replicative Life Span in the Budding Yeast. *J Vis Exp* (2009). doi:10.3791/1209
5. McCormick, M. A. *et al.* A Comprehensive Analysis of Replicative Lifespan in 4,698 Single-Gene Deletion Strains Uncovers Conserved Mechanisms of Aging. *Cell Metabolism* **22**, 895–906 (2015).
6. Lee, S. S., Vizcarra, I. A., Huberts, D. H. E. W., Lee, L. P. & Heinemann, M. Whole lifespan microscopic observation of budding yeast aging through a microfluidic dissection platform. *PNAS* **109**, 4916–4920 (2012).
7. Jo, M. C., Liu, W., Gu, L., Dang, W. & Qin, L. High-throughput analysis of yeast replicative aging using a microfluidic system. *PNAS* **112**, 9364–9369 (2015).
8. Zhang, Y. *et al.* Single Cell Analysis of Yeast Replicative Aging Using a New Generation of Microfluidic Device. *PLoS ONE* **7**, e48275 (2012).
9. Crane, M. M., Clark, I. B. N., Bakker, E., Smith, S. & Swain, P. S. A Microfluidic System for Studying Ageing and Dynamic Single-Cell Responses in Budding Yeast. *PLoS ONE* **9**, e100042 (2014).

10. Xie, Z. *et al.* Molecular phenotyping of aging in single yeast cells using a novel microfluidic device: Molecular phenotyping of aging. *Aging Cell* **11**, 599–606 (2012).
11. Fehrmann, S. *et al.* Aging Yeast Cells Undergo a Sharp Entry into Senescence Unrelated to the Loss of Mitochondrial Membrane Potential. *Cell Reports* **5**, 1589–1599 (2013).
12. Elvira, K. S., i Solvas, X. C., Wootton, R. C. R. & deMello, A. J. The past, present and potential for microfluidic reactor technology in chemical synthesis. *Nat Chem* **5**, 905–915 (2013).
13. Sackmann, E. K., Fulton, A. L. & Beebe, D. J. The present and future role of microfluidics in biomedical research. *Nature* **507**, 181–189 (2014).
14. Mettetal, J. T., Muzzey, D., Gómez-Uribe, C. & Oudenaarden, A. van. The Frequency Dependence of Osmo-Adaptation in Saccharomyces cerevisiae. *Science* **319**, 482–484 (2008).
15. Bennett, M. R. & Hasty, J. Microfluidic devices for measuring gene network dynamics in single cells. *Nat Rev Genet* **10**, 628–638 (2009).
16. Hansen, A. S., Hao, N. & O'Shea, E. K. High-throughput microfluidics to control and measure signaling dynamics in single yeast cells. *Nat. Protocols* **10**, 1181–1197 (2015).
17. Charvin, G., Cross, F. R. & Siggia, E. D. A Microfluidic Device for Temporally Controlled Gene Expression and Long-Term Fluorescent Imaging in Unperturbed Dividing Yeast Cells. *PLoS ONE* **3**, e1468 (2008).
18. Ryley, J. & Pereira-Smith, O. M. Microfluidics device for single cell gene expression analysis in Saccharomyces cerevisiae. *Yeast* **23**, 1065–1073 (2006).
19. Liu, P., Young, T. Z. & Acar, M. Yeast Replicator: A High-Throughput Multiplexed Microfluidics Platform for Automated Measurements of Single-Cell Aging. *Cell Reports* **0**,

20. Rafelski, S. M. *et al.* Mitochondrial Network Size Scaling in Budding Yeast. *Science* **338**, 822–824 (2012).
21. Saarikangas, J. & Barral, Y. Protein aggregates are associated with replicative aging without compromising protein quality control. *eLife Sciences* **4**, e06197 (2015).
22. Xie, Z. *et al.* Early Telomerase Inactivation Accelerates Aging Independently of Telomere Length. *Cell* **160**, 928–939 (2015).
23. Meitinger, F. *et al.* A Memory System of Negative Polarity Cues Prevents Replicative Aging. *Cell* **159**, 1056–1069 (2014).
24. McVey, M., Kaeberlein, M., Tissenbaum, H. A. & Guarente, L. The Short Life Span of Saccharomyces cerevisiae sgs1 and srs2 Mutants Is a Composite of Normal Aging Processes and Mitotic Arrest Due to Defective Recombination. *Genetics* **157**, 1531–1542 (2001).
25. Xu, Z. *et al.* Two routes to senescence revealed by real-time analysis of telomerase-negative single lineages. *Nat Commun* **6**, 7680 (2015).
26. Hughes, A. L. & Gottschling, D. E. An early age increase in vacuolar pH limits mitochondrial function and lifespan in yeast. *Nature* **492**, 261–265 (2012).
27. Veatch, J. R., McMurray, M. A., Nelson, Z. W. & Gottschling, D. E. Mitochondrial Dysfunction Leads to Nuclear Genome Instability via an Iron-Sulfur Cluster Defect. *Cell* **137**, 1247–1258 (2009).
28. Lai, C.-Y., Jaruga, E., Borghouts, C. & Jazwinski, S. M. A Mutation in the ATP2 Gene Abrogates the Age Asymmetry Between Mother and Daughter Cells of the Yeast Saccharomyces cerevisiae. *Genetics* **162**, 73–87 (2002).
29. Scheckhuber, C. Q. *et al.* Reducing mitochondrial fission results in increased life span and fitness of two fungal ageing models. *Nat Cell Biol* **9**, 99–105 (2007).

30. Kaeberlein, M., Kirkland, K. T., Fields, S. & Kennedy, B. K. Genes determining yeast replicative life span in a long-lived genetic background. *Mechanisms of Ageing and Development* **126**, 491–504 (2005).
31. Kennedy, B. K., Austriaco, N. R. & Guarente, L. Daughter cells of Saccharomyces cerevisiae from old mothers display a reduced life span. *J Cell Biol* **127**, 1985–1993 (1994).
32. Klein, J. & Moeschberger, M. *Survival Analysis*. (Springer-Verlag, 2003).
33. Yang, J. *et al.* Cell size and growth rate are major determinants of replicative lifespan. *Cell Cycle* **10**, 144–155 (2011).
34. He, C. *et al.* Enhanced Longevity by Ibuprofen, Conserved in Multiple Species, Occurs in Yeast through Inhibition of Tryptophan Import. *PLOS Genet* **10**, e1004860 (2014).
35. Huberts, D. H. E. W. *et al.* Calorie restriction does not elicit a robust extension of replicative lifespan in Saccharomyces cerevisiae. *PNAS* **111**, 11727–11731 (2014).
36. Smith, E. D., Kennedy, B. K. & Kaeberlein, M. Genome-wide identification of conserved longevity genes in yeast and worms. *Mechanisms of Ageing and Development* **128**, 106–111 (2007).
37. Smith, E. D. *et al.* Quantitative evidence for conserved longevity pathways between divergent eukaryotic species. *Genome Res.* **18**, 564–570 (2008).
38. Ghavidel, A. *et al.* Rapid Nuclear Exclusion of Hcm1 in Aging Saccharomyces cerevisiae Leads to Vacuolar Alkalization and Replicative Senescence. *G3: Genes, Genomes, Genetics* **8**, 1579–1592 (2018).
39. Kaeberlein, M. Lessons on longevity from budding yeast. *Nature* **464**, 513–519 (2010).
40. Chen, K. L., Crane, M. M. & Kaeberlein, M. Microfluidic technologies for yeast replicative lifespan studies. *Mechanisms of Ageing and Development* **161, Part B**, 262–269 (2017).

41. Li, Y. *et al.* Multigenerational silencing dynamics control cell aging. *Proceedings of the National Academy of Sciences* **114**, 11253–11258 (2017).

42. Janssens, G. E. *et al.* Protein biogenesis machinery is a driver of replicative aging in yeast. *eLife Sciences* e08527 (2015). doi:10.7554/eLife.08527

43. Liu, P. & Acar, M. The generational scalability of single-cell replicative aging. *Science Advances* **4**, eaao4666 (2018).

44. Denoth-Lippuner, A., Krzyzanowski, M. K., Stober, C. & Barral, Y. Role of SAGA in the asymmetric segregation of DNA circles during yeast ageing. *eLife Sciences* **3**, e03790 (2014).

45. Jin, M. *et al.* Divergent Aging of Isogenic Yeast Cells Revealed through Single-Cell Phenotypic Dynamics. *cels* **8**, 242-253.e3 (2019).

46. McDonald, J. C. *et al.* Fabrication of microfluidic systems in poly(dimethylsiloxane). *Electrophoresis* **21**, 27–40 (2000).

47. Pitrone, P. G. *et al.* OpenSPIM: an open-access light-sheet microscopy platform. *Nature Methods* **10**, 598–599 (2013).

48. Rosenegger, D. G., Tran, C. H. T., LeDue, J., Zhou, N. & Gordon, G. R. A High Performance, Cost-Effective, Open-Source Microscope for Scanning Two-Photon Microscopy that Is Modular and Readily Adaptable. *PLOS ONE* **9**, e110475 (2014).

49. Campbell, R. A. A., Eifert, R. W. & Turner, G. C. Openstage: A Low-Cost Motorized Microscope Stage with Sub-Micron Positioning Accuracy. *PLOS ONE* **9**, e88977 (2014).

50. Jawale, Y. K., Rapol, U. & Athale, C. A. Open Source 3D-printed focussing mechanism for cellphone-based cellular microscopy. *Journal of Microscopy* **273**, 105–114 (2019).

51. Switz, N. A., D'Ambrosio, M. V. & Fletcher, D. A. Low-Cost Mobile Phone Microscopy with a Reversed Mobile Phone Camera Lens. *PLOS ONE* **9**, e95330 (2014).

52. Orth, A., Wilson, E. R., Thompson, J. G. & Gibson, B. C. A dual-mode mobile phone microscope using the onboard camera flash and ambient light. *Scientific Reports* **8**, 3298 (2018).

53. Cybulski, J. S., Clements, J. & Prakash, M. Foldscope: Origami-Based Paper Microscope. *PLOS ONE* **9**, e98781 (2014).

54. Sharkey, J. P., Foo, D. C. W., Kabla, A., Baumberg, J. J. & Bowman, R. W. A one-piece 3D printed flexure translation stage for open-source microscopy. *Review of Scientific Instruments* **87**, 025104 (2016).

55. Schneidereit, D., Kraus, L., Meier, J. C., Friedrich, O. & Gilbert, D. F. Step-by-step guide to building an inexpensive 3D printed motorized positioning stage for automated high-content screening microscopy. *Biosensors and Bioelectronics* **92**, 472–481 (2017).

56. Song, R., Sarnoski, E. A. & Acar, M. The Systems Biology of Single-Cell Aging. *iScience* **7**, 154–169 (2018).

57. Martinez-Jimenez, C. P. *et al.* Aging increases cell-to-cell transcriptional variability upon immune stimulation. *Science* **355**, 1433–1436 (2017).

58. Chen, K. L., Crane, M. M. & Kaeberlein, M. Microfluidic technologies for yeast replicative lifespan studies. *Mechanisms of Ageing and Development* doi:10.1016/j.mad.2016.03.009

59. Li, S. C. & Kane, P. M. The yeast lysosome-like vacuole: Endpoint and crossroads. *Biochimica et Biophysica Acta (BBA) - Molecular Cell Research* **1793**, 650–663 (2009).

60. Carmona-Gutierrez, D., Hughes, A. L., Madeo, F. & Ruckenstuhl, C. The crucial impact of lysosomes in aging and longevity. *Ageing Research Reviews* **32**, 2–12 (2016).

61. Perera, R. M. & Zoncu, R. The Lysosome as a Regulatory Hub. *Annual Review of Cell and Developmental Biology* **32**, 223–253 (2016).

62. Baxi, K., Ghavidel, A., Waddell, B., Harkness, T. A. & Carvalho, C. E. de. Regulation of Lysosomal Function by the DAF-16 Forkhead Transcription Factor Couples Reproduction to Aging in Caenorhabditis elegans. *Genetics* **207**, 83–101 (2017).

63. Huh, W.-K. *et al.* Global analysis of protein localization in budding yeast. *Nature* **425**, 686–691 (2003).

64. Matthew John, M. pHluorin2: an enhanced, ratiometric, pH-sensitive green florescent protein. *Advances in Bioscience and Biotechnology* **2011**, (2011).

65. Inoue, H., Noumi, T., Nagata, M., Murakami, H. & Kanazawa, H. Targeted disruption of the gene encoding the proteolipid subunit of mouse vacuolar H+-ATPase leads to early embryonic lethality. *Biochimica et Biophysica Acta (BBA) - Bioenergetics* **1413**, 130–138 (1999).

66. Diab, H. I. & Kane, P. M. Loss of Vacuolar H+-ATPase (V-ATPase) Activity in Yeast Generates an Iron Deprivation Signal That Is Moderated by Induction of the Peroxiredoxin TSA2. *J Biol Chem* **288**, 11366–11377 (2013).

67. Liao, C., Hu, B., Arno, M. J. & Panaretou, B. Genomic Screening in Vivo Reveals the Role Played by Vacuolar H+ ATPase and Cytosolic Acidification in Sensitivity to DNA-Damaging Agents Such as Cisplatin. *Mol Pharmacol* **71**, 416–425 (2007).

68. Philpott, C. C. & Smith, P. M. Iron Starvation Response in Saccharomyces cerevisiae. in *Encyclopedia of Inorganic and Bioinorganic Chemistry* 1–16 (American Cancer Society, 2013). doi:10.1002/9781119951438.eibc2132

69. Chen, O. S. *et al.* Transcription of the Yeast Iron Regulon Does Not Respond Directly to Iron but Rather to Iron-Sulfur Cluster Biosynthesis. *J. Biol. Chem.* **279**, 29513–29518 (2004).

70. Lill, R. *et al.* The role of mitochondria in cellular iron–sulfur protein biogenesis and iron metabolism. *Biochimica et Biophysica Acta (BBA) - Molecular Cell Research* **1823**, 1491–1508 (2012).

71. Kispal, G. *et al.* Biogenesis of cytosolic ribosomes requires the essential iron–sulphur protein Rli1p and mitochondria. *The EMBO Journal* **24**, 589–598 (2005).

72. Pal, S., Postnikoff, S. D., Chavez, M. & Tyler, J. K. Impaired cohesion and homologous recombination during replicative aging in budding yeast. *Science Advances* **4**, eaaq0236 (2018).

73. Lindstrom, D. L., Leverich, C. K., Henderson, K. A. & Gottschling, D. E. Replicative Age Induces Mitotic Recombination in the Ribosomal RNA Gene Cluster of Saccharomyces cerevisiae. *PLoS Genetics* **7**, e1002015 (2011).

74. Hu, Z. *et al.* Ssd1 and Gcn2 suppress global translation efficiency in replicatively aged yeast while their activation extends lifespan. *eLife* (2018). doi:10.7554/eLife.35551

75. Pijuan, J., Maria, C., Herrero, E. & Belli, G. Impaired mitochondrial Fe-S cluster biogenesis activates the DNA damage response through different signaling mediators. *Journal of Cell Science* **128**, 4653–4665 (2015).

76. Díaz de la Loza, M. del C. *et al.* Zim17/Tim15 links mitochondrial iron–sulfur cluster biosynthesis to nuclear genome stability. *Nucleic Acids Res* **39**, 6002–6015 (2011).

77. Alvaro, D., Lisby, M. & Rothstein, R. Genome-Wide Analysis of Rad52 Foci Reveals Diverse Mechanisms Impacting Recombination. *PLOS Genetics* **3**, e228 (2007).

78. Gasior, S. L., Wong, A. K., Kora, Y., Shinohara, A. & Bishop, D. K. Rad52 associates with RPA and functions with Rad55 and Rad57 to assemble meiotic recombination complexes. *Genes & Development* **12**, 2208–2221 (1998).

79. Lisby, M., Rothstein, R. & Mortensen, U. H. Rad52 forms DNA repair and recombination centers during S phase. *PNAS* **98**, 8276–8282 (2001).

80. Novarina, D. *et al.* Increased genome instability is not accompanied by sensitivity to DNA damaging agents in aged yeast cells. *DNA Repair* **54**, 1–7 (2017).

81. Netz, D. J. A., Mascarenhas, J., Stehling, O., Pierik, A. J. & Lill, R. Maturation of cytosolic and nuclear iron–sulfur proteins. *Trends in Cell Biology* **24**, 303–312 (2014).

82. Miles, A. L., Burr, S. P., Grice, G. L. & Nathan, J. A. The vacuolar-ATPase complex and assembly factors, TMEM199 and CCDC115, control HIF1α prolyl hydroxylation by regulating cellular iron levels. *eLife* **6**, e22693 (2017).

83. Teo, Y. V. *et al.* Notch Signaling Mediates Secondary Senescence. *Cell Reports* **27**, 997-1007.e5 (2019).

84. Enge, M. *et al.* Single-Cell Analysis of Human Pancreas Reveals Transcriptional Signatures of Aging and Somatic Mutation Patterns. *Cell* **171**, 321-330.e14 (2017).

85. Bahar, R. *et al.* Increased cell-to-cell variation in gene expression in ageing mouse heart. *Nature* **441**, 1011–1014 (2006).

86. Vuong, N. H. *et al.* Single-cell RNA-sequencing reveals transcriptional dynamics of estrogen-induced dysplasia in the ovarian surface epithelium. *PLOS Genetics* **14**, e1007788 (2018).

87. Rouault, T. A. & Tong, W. H. Iron–sulfur cluster biogenesis and human disease. *Trends in Genetics* **24**, 398–407 (2008).

88. Rychtarcikova, Z. *et al.* Tumor-initiating cells of breast and prostate origin show alterations in the expression of genes related to iron metabolism. *Oncotarget* **8**, 6376–6398 (2016).

89. Nasmyth, K. A. & Reed, S. I. Isolation of genes by complementation in yeast: molecular cloning of a cell-cycle gene. *PNAS* **77**, 2119–2123 (1980).

90. Alberti, S., Gitler, A. D. & Lindquist, S. A suite of Gateway® cloning vectors for high-throughput genetic analysis in Saccharomyces cerevisiae. *Yeast* **24**, 913–919 (2007).

91. Wasko, B. M., Holland, C. L., Resnick, M. A. & Lewis, L. K. Inhibition of DNA double-strand break repair by the Ku heterodimer in mrx mutants of Saccharomyces cerevisiae. *DNA Repair (Amst)* **8**, 162–169 (2009).

92. Tong, W.-H. & Rouault, T. A. Functions of mitochondrial ISCU and cytosolic ISCU in mammalian iron-sulfur cluster biogenesis and iron homeostasis. *Cell Metabolism* **3**, 199–210 (2006).